University of Alabama in Huntsville

LOUIS

2017

A closed-form solution to the aeroelastic response of an elastic plate in axial flow

Cory Ryan Medina

Follow this and additional works at: https://louis.uah.edu/uah-theses

A CLOSED-FORM SOLUTION TO THE AEROELASTIC

RESPONSE OF AN ELASTIC PLATE IN AXIAL FLOW

by

CORY RYAN MEDINA

A THESIS

Submitted in partial fulfillment of the requirements
for the degree of Master of Science in Engineering
in
The Department of Mechanical and Aerospace Engineering
to
The School of Graduate Studies
of
The University of Alabama in Huntsville

HUNTSVILLE, ALABAMA

2017

In presenting this thesis in partial fulfillment of the requirements for a master degree from The University of Alabama in Huntsville, I agree that the Library of this University shall make it freely available for inspection. I further agree that permission for extensive copying for scholarly purposes may be granted by my advisor or, in his/her absence, by the Chair of the Department or the Dean of the School of Graduate Studies. It is also understood that due recognition shall be given to me and to The University of Alabama in Huntsville in any scholarly use which may be made of any material in this thesis.
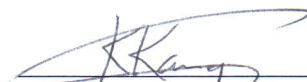
_____   11/7/2017
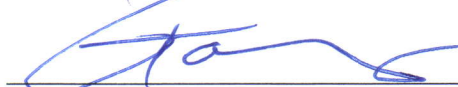(student signature)   (date)

THESIS APPROVAL FORM

Submitted by Cory Ryan Medina in partial fulfillment of the requirements for the degree of Masters of Science in Engineering and accepted on behalf of the Faculty of the School of Graduate Studies by the thesis committee.
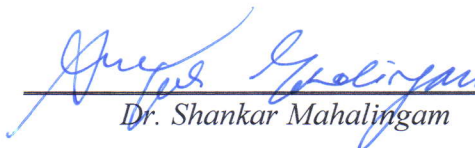
We, the undersigned members of the Graduate Faculty of The University of Alabama in Huntsville, certify that we have advised and/or supervised the candidate on the work described in this thesis. We further certify that we have reviewed the thesis manuscript and approve it in partial fulfillment of the requirements for the degree of Master of Science in Engineering.

Dr. Chang-kwon Kang	11/1/2017 (Date)	Committee Chair
Dr. D. Brian Landrum	11/1/2017 (Date)	
Dr. Gang Wang	11/1/2017 (Date)	
Dr. D. Keith Hollingsworth	11/3/17 (Date)	Department Chair
Dr. Shankar Mahalingam	11/06/17 (Date)	College Dean
Dr. David Berkowitz	11/13/17 (Date)	Graduate Dean

III

ABSTRACT

School of Graduate Studies
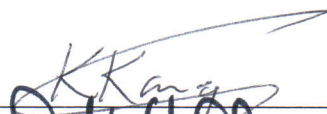The University of Alabama in Huntsville
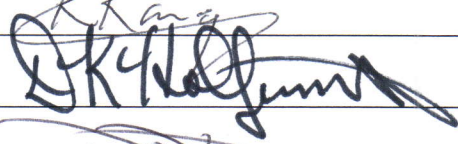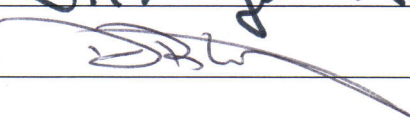
Degree <u>Master of Science in Engineering</u>   College/Dept. <u>Engineering/Mechanical and Aerospace Engineering</u>

Name of Candidate <u>Cory Ryan Medina</u>

Title <u>A Closed-Form Solution to the Aeroelastic Response of an Elastic Plate in Axial Flow</u>

The unsteady aeroelastic response of an elastic plate immersed in an axial flow addresses many real-world applications and problems from plate flutter, bio-locomotion, to deforming airfoils. However, the analysis is challenging due to the coupling between the structure and fluid. This study presents a closed-form analytical solution to the two-way coupled aeroelastic response of a two-dimensional elastic plate in axial potential flow. The coupled model utilizes linearized beam theory and linearized unsteady thin airfoil theory. The coupled equations of motion are solved via Galerkin's method, where closed-form solutions for the plate deformation are obtained by introducing Chebyshev series to solve the unsteady aerodynamics. Furthermore, closed-form solutions are obtained for the lift, thrust and power. The model is validated against results found in the literature and show

good agreement. Furthermore, we present a study on the effect of chordwise flexibility on the aerodynamic performance for a typical biological flyer in forward flight.

Abstract Approval: Committee Chair _____

Department Chair _____

Graduate Dean _____

V

TABLE OF CONTENTS

Page

LIST OF FIGURES

LIST OF TABLES

LIST OF SYMBOLS

A	Beam cross sectional area	m^2
b	Mid-chord	m
$C(k)$	Theodorsen's function	
c	Chord	m
c_n	Chebyshev coefficient	
E	Young's modulus	N/m^2
F	Real component of Theodorsen's function	
f	Frequency	Hz
G	Imaginary component of Theodorsen's function	
H_n	Hankel function	
h	Plunge displacement	m
h_a	Plunge amplitude	m
h_s	Beam thickness	m
I	Beam second moment of inertia	m^4
i	Imaginary number	
i	Index value	
J_n	Bessel function of the first kind	
j	Index value	
k	Reduced frequency	
L	Lift	N
P	Power	$N/m\text{-}s$
p	Pressure	N/m^2
Q	Generalized aerodynamic force	N/m
q	Fourier coefficient	
Re	Reynold's number	
S	Summation of Chebyshev coefficients	
St	Strouhal number	
T	Thrust	N
T_n	Chebyshev polynomial of the first kind	
t	Time	s
U_∞	Free stream flow speed	m/s
v	Total displacement	m
w	Plate deformation	m
X	X-coordinate in the XY-plane	m
x	x-coordinate in the xy-plane	m
Y	Y-coordinate in the XY-plane	m
Y_n	Bessel function of the second kind	
y	y-coordinate in the xy-plane	m

$()^*$	Normalized variable	
Γ	Vortex strength	
ε	Frequency error	Hz
ζ	Constant	
η	Generalized aerodynamic force term	
κ	Generalized aerodynamic force term	
λ	Beam eigenvalue	
μ	Generalized aerodynamic force term	
Π_0	Effective mass	
Π_1	Effective stiffness	
ρ_f	Fluid density	kg/m^3
ρ_s	Beam density	kg/m^3
σ	Source/sink strength	m/s
τ	Beam temporal solution	
φ	Phase angle	rad
ϕ	Velocity potential	m^2/s
ψ	Beam normal function	

CHAPTER 1

INTRODUCTION

1.1   Background and Motivation

Aeroelasticity is the study of the mutual interaction between inertia, elastic and aerodynamic forces [1]. Although this topic covers a wide range of applications, in this work we focus on the unsteady aeroelastic response of a thin elastic plate immersed in an axial flow. Such a problem addresses many real-world applications and problems. Wings of birds, bats, and insects deform significantly during flight [2]. However, this fluid-structure interaction (FSI) mechanism is difficult to understand due to the involved physics. Earlier studies have shown that wing deformation can enhance thrust generation while reducing power consumption [3,4]. Because of this, researchers are interested in understanding the FSI mechanism of flapping wings to improve propulsion efficiency of future Micro Aerial Vehicles (MAVs). In-flight adaptive morphing wings are now feasible with the recent development of advanced composites as well as sensor and actuator technologies [5]. Morphing wings can improve aircraft operation efficiency by passively or actively changing the contour shape tailored for different flight conditions [5]. However, passive

camber deformation can be susceptible to aeroelastic instability [6]. Understanding this aeroelastic mechanism can help improve future morphing wing design. In turbomachinery, characterizing the aeroelastic damping on inducer blades has become of high interest as new designs seek to be more efficient, consequently resulting in more aggressive operating conditions, potentially operating near resonance [7]. Without a proper prediction of the hydrodynamic damping, calculated inducer blade responses would intolerably escalate. Furthermore, understanding the aeroelastic response of elastic plates can aid the research in energy harvesting as well as understanding the mechanism of snoring in humans [8].

To determine the aeroelastic response of a plate under forced or self-excitation, the plate inertia, elastic restoring force and aerodynamic forces must be dynamically balanced. One of the interesting aspects of this problem is the two-way coupling between the structural response and the aerodynamic forces. The aerodynamics depend on the plate dynamics. However, to determine the plate motion the loading must be known, and hence, the two models are tightly coupled directly depending on one another. The main challenge of this problem is obtaining the unsteady aerodynamics for a deformable plate as a function of the main unknowns from the structural model, so that the combined coupled equations of motion can be solved using known analytical methods. Other challenges of such a problem arise due to three-dimensional effects, viscous flow effects, and nonlinear effects. Nearly all Newtonian fluids are viscous, governed by the Navier-Stokes equation. However, inviscid approximation can provide adequate solutions for high Reynold number flows or for flows that are attached outside the boundary layer [9]. Although all flows are three-dimensional in nature, two-dimensional models can give a good approximation for when the aerodynamics are dominantly changing in a single plane. For instance, this behavior is observed in the chordwise direction of high aspect ratio wings in forward flight and away from the wing tip.

Nonlinear effects can occur at large deformations, however, linear approximation can yield good results in the domain of small deformations. Although the above simplifications and assumptions are enforced, such a simplified model can aid in the fundamental understanding of FSI mechanisms by highlighting the first-order physical mechanisms.

Solutions for the unsteady aerodynamics of chordwise deformable airfoils have been presented by Wu [10], Peters et al. [11], and Walker [11-13]. Walker [11,12], who presents closed-form solutions by introducing a Chebyshev expansion, investigates the effect chordwise curvature has on the aerodynamic parameters of lift and thrust. However, this work is based on prescribed deformation. Walker [14] extends this work by investigating the propulsion efficiency due to chordwise curvature and applying this aerodynamic model to the dynamic response of a two-dimensional membrane. Although this membrane model includes the effect of inertia and aerodynamic forces, it does not account for the elastic restoring force. Extending the work done by Walker [11-13], we obtain a closed-form expression for the transient response for the two-dimensional elastic plate in axial flow, including the effects of inertia, elastic, and aerodynamic forces.

This aeroelastic problem has been investigated using analytical, semi-analytical, numerical and experimental techniques. Sophisticated numerical simulations and experimental results can yield instantaneous information of the flow and plate dynamics; however, analytical models can yield results faster at less expense. Although final designs may revert to sophisticated numerical codes to accurately predict the aeroelastic response, analytical solutions can provide quick and efficient predictions for initial design studies within a large trade-space. Furthermore, analytical solutions have the key ability to provide relationships between various physical parameters involved in the FSI. Knowledge of these relationships can aid in the fundamental understanding

of the aeroelastic mechanisms and aid in optimization. Because of these benefits, this research has focused on improving the analytical tools to this problem. Although analytical models have been developed, to our knowledge, a closed-form analytical solution to this two-way coupled FSI problem has not been presented in the literature.

1.2   Objective

The objective of this research is to develop a closed-form analytical solution to the two-way coupled, two-dimensional unsteady aeroelastic response of an elastic plate immersed in an axial flow within the linear framework. The coupled model utilizes the linearized beam theory for the structural model and thin airfoil theory, which assumes incompressible potential flow, for the aerodynamic model. Implementing Galerkin's method, the plate deformation is expressed as the linear summation of the known beam normal functions and unknown temporal solutions. By deriving the unsteady aerodynamic pressure with respect to the beam normal functions, which is further expressed in a Chebyshev polynomial expansion, the generalized aerodynamic load is expressed in closed-form. Utilizing the orthogonality relationship of the normal functions, the equations of motion reduce to N number of coupled second-order ordinary differential equations with the temporal solution as the unknown variable. The coupled equations of motion can be solved using existing analytical methods. Furthermore, closed-form solutions are obtained for the lift force, generated thrust, required input power and propulsion efficiency. To prove the validity of the model we compare the results of the current model to results published in the literature. Furthermore, we investigate the effect of mode contribution on the solution. This work primarily focuses on the application of flutter and flapping wings, which utilize the cantilever beam configuration. The novel contribution of this work is presenting the analytical solution to the two-way coupled, two-dimensional unsteady aeroelastic response of an elastic plate immersed in axial

potential flow in a closed-form. The anticipation of doing so, is to aid in the understanding of the aeroelastic mechanisms and encourage future implications of this solution in future applications, such as design studies, three-dimensional models or in-flight controls, due to its simplistic solution form.

1.3 Literature Survey

As early as the 1800's, researchers have been intrigued by this fluid-structure interaction phenomenon. One of the earliest published works was by Lord Rayleigh [15] who theoretically proved that a flag of infinite dimension is always unstable when subjected to flow.

Aeroelasticity became an important research topic during World War I, when airplanes unknowingly started to operate near their flutter speeds. By 1935, the mechanism of potential flow flutter was sufficiently understood for rigid airfoils undergoing rigid body motion, which was attributed by Glauert [16], Frazer and Duncan [17], Küssner [18], and Theodorsen [19]. As airplanes entered the realm of supersonic and hypersonic flight, panel flutter became an issue causing excessive noise and damage to the aircraft [20]. Unlike the theory developed for rigid airfoils undergoing rigid body motion, panel flutter involves thin plates undergoing higher order bending subjected to flow only on one side. Panel flutter mainly occurred during high speed flight, and therefore, the majority of the research considered the assumptions of supersonic compressible flow. During the 1950's and 1960's the theory for supersonic panel flutter was fairly well established through several published papers: Miles [21] introduced a traveling wave theory for an infinite panel, where he assumed stagnate air on the other side. Using a Rayleigh type analysis, Nelson & Cunningham [22] developed a model using acoustical theory to model the stagnate air on the other side. Eisley [23] solved the three-dimension model by using strip theory and Hedgepeth [24] improved it by replacing the strip theory with a Galerkin's solution. Dowell [25]

solved the problem for a finite panel and Dugundi et al. [26] extended this work by replacing the still air with an elastic foundation.

Aeroelasticity also became a problem in the energy industry during the 1940's when reactor-fuel-plates collapsed when the coolant flow was increased to sufficiently high velocities. This initiated research in subsonic aeroelastic instability of parallel-plate assemblies. These parallel-plate assemblies are used as core elements in some nuclear reactors. Unlike the panel flutter problem, the plates experienced subsonic flow on both sides of the plate and may experience dynamic coupling due to neighboring plates. These assemblies consist of long thin plates stacked in parallel containing a gap between them, allowing cooling fluid to flow between them. In a situation when the flow speed becomes sufficiently high, the plates collapse due to either static or dynamic instability, resulting in failure of the reactor [27]. The first model to predict static instability was presented by Miller [27], who used Bernoulli's theorem to equate the pressure difference between the channels to the elastic restoring force of the plates. Johansson [28] and others further improved Millers [27] static model. A dynamic model was developed by Rosenberg and Yougdahl [29] which obtained the same critical velocity as Miller [27]. Guo & Païdoussis [30] present a more accurate and general analysis to this problem, using Fourier series to obtain the perturbation pressure from the two-dimensional incompressible potential flow equations. Recent studies, such as Schouveiler [31] and Michelin [32] have investigated the coupling effect on mode shapes due to neighboring parallel plates.

Unlike the panel and parallel plate assembly models, only a single plate is considered in this study subjected to flow on both sides and accounting for the unsteadiness of the flow by including a wake shed at the trailing-edge. This configuration has been used to model various scenarios. Although primarily focused on panel flutter, Kornecki et al. [33] investigates the flutter

boundary of this configuration, comparing results to experimental data. Huang [8] chose to use this configuration to study the human soft palate that causes snoring. In response to the occurrence of paper flutter in printing presses, which resulted in lower quality and a decrease in production, Watanabe et al. [34] investigated the aeroelastic stability of paper using analytical, numerical and experimental techniques. Guo & Païdoussis [35] also developed a model for a single plate flutter in channel flow, using the same model approach as in their parallel-plate model [30], just with different boundary conditions. Using a semi-analytical model, Breuker et al. [6], investigated the effects of a stiff leading-edge on the stability boundary of morphing wings. All these analytical and semi-analytical models are similar, utilizing linear beam theory to model the structure, however, they differ in the selection of the aerodynamic model. Kornecki et al. [33] and Breuker et al. [6] used Theodorsen's [19] aerodynamic theory with Glauert's Fourier expansion; Huang [8] used Theodorsen's [19] aerodynamic theory solved numerically; Watanabe et al. [34] used the aerodynamic theory by Küssner [18]; and Guo & Païdoussis [35] use Fourier series to directly solve the potential flow equations. Although the aerodynamic theory differed between these models, the mathematics behind their solutions are alike, implementing Fourier series. Furthermore, none of them present closed-form solutions to the dynamic response of the plate and do not investigate the aerodynamic performance, such as lift, thrust and power.

This two-dimensional problem has been studied using numerical models by Yadykin et al. [36], Tang & Païdoussis [37], Alben et al. [38], Howell et al. [39], and Michelin et al. [40]. Three-dimensional effects have been studied by several researchers. Eloy [41] extends the work done by Guo & Païdoussis [35] by adapting their solution to account for finite span. Extending the work done by Eloy [41], Doaré et al. [42] investigate spanwise tip edge clearances to the channel wall. However, in doing so, the wake is neglected resulting in a quasi-steady solution. Gibbs et al. [43]

studies the stability boundary for various different boundary conditions using a three-dimensional numerical model.

A special case of this problem can be used to simulate the chordwise dynamics of flapping wings in forward flight. Here, the interest is on aerodynamic performance rather than aeroelastic stability. This problem has been studied primarily through experiments and numerical models. Only recently has this problem been studied analytically. Inspired by the early experimental results published by Heathcote and Gursul [37,38], Kang et al. [3] studied the effects of chordwise flexibility on the aerodynamic performance of flapping wings using a Navier-Stokes numerical solver. The same problem was studied analytically by Kodali [46], who coupled the solutions for the Euler-Bernoulli beam and Theodorsen's [19] solution for rigid airfoils. The lift force is obtained by approximating the first bending mode by a rigid plate with passive pitch, realizing that the passive pitch is equal to the angle of attack. By assuming a harmonic motion, a closed-form analytical solution for the trailing-edge displacement is obtained. Although this model does not take into account any plate curvature in the aerodynamics, Kodali [46] shows good agreement when compared to experimental and numerical results for when the deformations are small. The flapping wing solution in Section 3.3.2 can be seen as an extension of this work, for it accounts for plate curvature in the aerodynamics. Similar to Kodali's approach [46], Moore [47] presents an analytical model utilizing a rigid wing with a torsional spring at the leading-edge which is allowed to passively pitch. Moore [48] extends this work by presenting a semi-analytical model to study the optimal configuration for thrust production. Utilizing the Euler-Bernoulli beam and Küssner's [18] aerodynamic theory, the coupled model is solved numerically using a Chebyshev collocation method. Although this model accounts for plate curvature in the aerodynamic loading,

8

it requires to be solved numerically. Other numerical models have been presented by Alben [49] and Michelin et al. [50].

1.4   Outline

In Chapter 1, the background and motivation for this research was presented, along with the literature review of the past and resent work performed on this subject matter. In Chapter 2, the methodology for the structural dynamics and aerodynamics will be derived in detail along with the two-way coupled equation of motion. In Chapter 3, we present the solution to the two-way coupled aeroelastic equation of motion in closed-form expressions along with closed-form expressions for the lift force, generated thrust and input power. In Chapter 4 we introduce the details of the cantilever beam, followed by a validation of the current model's results to results found in the literature along with a discussion of similarities and differences. We continue results by studying the effect of mode contribution on the solution by investigating the chordwise flexibility on the aerodynamic performance of an average biological flyer in forward flight. We will close this study with conclusions, a list of novel contributions and future work in Chapter 5. Appendices A through C contain supplemental information used in the main text. Appendix D contains the Mathematica script used to derive the solutions for the unsteady aerodynamics.

CHAPTER 2

METHODOLOGY

2.1   Case Set-Up

For this two-dimensional model, we consider a thin elastic plate with infinite span and finite chord, $c=2b$, in a uniform freestream flow, U_∞, as shown in Figure 2.1. We consider a high Reynolds number (Re) flow, where the inertia forces in the surrounding fluid are important and the viscous effects are only important in the generation of circulation around the plate. To model the high Re flow, we treat the fluid as inviscid, but account for the viscous production of vorticity within boundary layers by allowing the plate to shed a vortex sheet from its trailing-edge [51]. We allow an impose forcing function in the form of a plunge base excitation, $h(t)$, where t is the time variable. The inertia force causes the plate to deform to an arbitrary deformation, $w(x,t)$, generating a pressure difference, $\Delta p(x,t)$, on the plate. What makes this problem challenging is the two-way coupling between the structure and the fluid. To determine the unsteady pressure the plate dynamics must be known. However, to determine the plate dynamics the unsteady pressure must be known, and hence, the two are tightly coupled directly depending on one another.
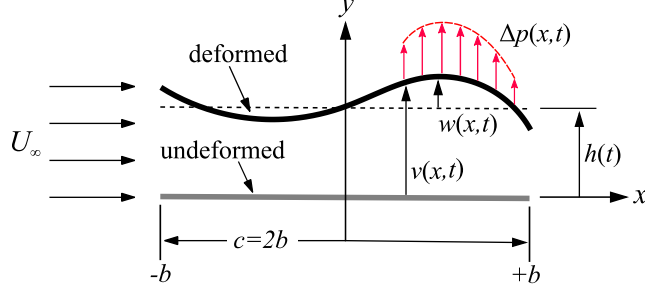
Figure 2.1. Schematic describing the current study case setup of an elastic plate in axial flow.

The instantaneous total displacement, $v(x,t)$ of the plate can be described as the sum of the instantaneous plate deformation $w(x,t)$ and the plunge motion $h(t)$, such that

$$v(x,t) = w(x,t) + h(t). \tag{2.1}$$

To linearize the problem, we enforce that the plate displacements are small relative to the chord, such that $|w| \ll c$ and $|h| \ll c$.

Up to this point we have not enforced any restrictions on the boundary conditions of the beam, which will be discussed in the next section. The structural dynamics of such a configuration can be represented by the governing equations of the transient linear Euler Bernoulli beam. The pressure difference generated on the plate can be determined by utilizing the unsteady thin airfoil theory for deformable airfoils as proposed by Walker [13], which is an extension to the aerodynamic theory developed by Theodorsen [19] for rigid airfoils.

11

2.2   Structural Methodology

2.2.1   Euler-Bernoulli Beam

The plate is modeled as a one-dimensional linear Euler-Bernoulli beam, for which the governing differential equation for the transverse dynamic response is given as,

$$\rho_s A \frac{\partial^2 v}{\partial t^2} + EI \frac{\partial^4 v}{\partial x^4} = \ell \Delta p, \qquad (2.2)$$

where ρ_s is the plate density, A is the cross-sectional area, E is the Young's modulus, I is the second moment of inertia, ℓ is the plate width, v is the transverse displacement and Δp is the pressure difference acting on the beam. As mentioned earlier, the total transverse displacement can be written as the sum of the plate deformation and the plunge base excitation. Let us prescribe a harmonic base excitation given as,

$$h(t) = h_a \left(e^{i2\pi ft} - 1 \right), \qquad (2.3)$$

where i is the imaginary unit, f is the plunging frequency and h_a is the plunge amplitude, where $h_a \ll c$ in order to satisfy the small perturbation assumption in both Euler-Bernoulli beam theory and thin airfoil theory. Substituting Eq. (2.1) and Eq. (2.3) into Eq. (2.2) yields the governing differential equation of motion as a function of the plate deformation, expressed as,

$$\rho_s A \frac{\partial^2 w}{\partial t^2} + EI \frac{\partial^4 w}{\partial x^4} = \ell \Delta p - \rho_s A \frac{d^2 h}{dt^2}. \qquad (2.4)$$

The second term on the right-hand side appears from the inertia force due to the imposed plunge base excitation which is a function of time only.

2.2.2 Nondimensional Equation of Motion

The governing equation of motion is normalized with $\rho_f U_\infty c$. Introducing the definitions for the cross-sectional area, $A = \ell h_s$, and the moment of inertia, $I = \ell h_s^3/12$, where h_s is the plate thickness, Eq. (2.4) can be written as,

$$\frac{\rho_s \ell h_s}{\rho_f U_\infty^2 c} \frac{\partial^2 w}{\partial t^2} + \frac{E\ell h_s^3}{12\rho_f U_\infty^2 c} \frac{\partial^4 w}{\partial x^4} = \frac{\ell}{\rho_f U_\infty^2 c} \Delta p - \frac{\rho_s \ell h_s}{\rho_f U_\infty^2 c} \frac{d^2 h}{dt^2} \,. \qquad (2.5)$$

Table 2.1. Nondimensional parameters.

Parameter	Definition
normalized spatial unit, x^*	x/b
normalized temporal unit, t^*	ft
normalized plate deformation, w^*	w/b
normalized plunge motion, h^*	h/b
thickness ratio, h_s^*	h_s/c
density ratio, ρ^*	$\rho s/\rho_f$
reduced frequency, k	$\pi fc/U_\infty$

Introducing the non-dimensional parameters given in Table 2.1, Eq. (2.5) can be written as

$$\rho^* h_s^* \left(\frac{k}{\pi}\right)^2 \frac{\partial^2 w^*}{\partial t^{*2}} + 16 \left(\frac{Eh_s^{*3}}{12\rho_f U_\infty^2}\right) \frac{\partial^4 w^*}{\partial x^{*4}} = 2\Delta p^* - \rho^* h_s^* \left(\frac{k}{\pi}\right)^2 \frac{d^2 h^*}{dt^{*2}} \,, \qquad (2.6)$$

where $\Delta p^* = \Delta p / \rho_f U_\infty^2$ is the normalized pressure difference. It is worth noting that the values 16 and 2 appear in the stiffness term and pressure term, respectively, due to normalizing the spatial unit, x, by the semi-chord, b, instead of the chord, c. This is intentionally done to aid in the solution of the aerodynamics which is typically described in terms of b. We introduce the effective inertia [3], $\Pi_0 = \rho^* h_s^* (k/\pi)^2$ and the effective stiffness [3], $\Pi_1 = Eh_s^{*3}/12\rho_f U_\infty^2$, so that the complete non-dimensional form of the governing differential equation of motion can be written as,

$$\Pi_0 \frac{\partial^2 w^*}{\partial t^{*2}} + 16\Pi_1 \frac{\partial^4 w^*}{\partial x^{*4}} = 2\Delta p^* - \Pi_0 \frac{d^2 h^*}{dt^{*2}} . \tag{2.7}$$

2.2.3   Solution via Galerkin's Method

Applying the Galerkin's method, the plate deformation can be written as a summation of the products of the known beam normal function, $\psi_i(x^*)$, and unknown temporal solutions, $\tau_i(t^*)$. Therefore, we can write w^* as,

$$w^*\left(x^*,t^*\right) = \sum_{i=1}^{\infty} \psi_i\left(x^*\right)\tau_i\left(t^*\right), \tag{2.8}$$

where the subscript i indicates individual beam modes and the general beam normal functions are defined as [52],

$$\psi_i\left(x^*\right) = C_{1,i}\sin\left(\frac{\lambda_i}{2}\left(x^*+1\right)\right) + C_{2,i}\cos\left(\frac{\lambda_i}{2}\left(x^*+1\right)\right)$$
$$+ C_{3,i}\sinh\left(\frac{\lambda_i}{2}\left(x^*+1\right)\right) + C_{4,i}\cosh\left(\frac{\lambda_i}{2}\left(x^*+1\right)\right), \tag{2.9}$$

where the constants $C_{1,i}$, $C_{2,i}$, $C_{3,i}$, $C_{4,i}$ and λ_i are determined by satisfying the four boundary conditions at $x^*=-1$ and $x^*=1$. Changing the beam domain from the traditional $0 \leq x^* \leq 1$ to $-1 \leq x^* \leq 1$ is solely done to aid in the solution of the aerodynamics. Substituting Eq. (2.8) into Eq. (2.4) yields,

$$\Pi_0 \sum_{i=1}^{\infty} \psi_i \ddot{\tau}_i + 16\Pi_1 \sum_{i=1}^{\infty} \psi_i'''' \tau_i = 2\Delta p^* - \Pi_0 \ddot{h}^*, \tag{2.10}$$

where ($\dot{\ }$) and ($\ $)$'$ denote derivatives with respect to t^* and x^*, respectively. We now take advantage of the orthogonality property of the beam normal functions. First, we multiply both sides by another set of beam normal functions, indicated by subscript j, and integrate over the chord yielding

$$\sum_{i=1}^{\infty} \int_{-1}^{1} \left(\Pi_0 \psi_i \psi_j \ddot{\tau}_i + 16\Pi_1 \psi_i'''' \psi_j \tau_i \right) dx^* = \int_{-1}^{1} \left(2\Delta p^* - \Pi_0 \ddot{h}^* \right) \psi_j dx^*. \tag{2.11}$$

Due to the orthogonality, the fourth derivative of the beam normal function evaluates to, $\partial^4 \psi_i / \partial x^{*4} = (\lambda_i^4 / 16) \psi_i$. Substituting this into Eq. (2.11) yields,

$$\sum_{i=1}^{\infty} \int_{-1}^{1} \left(\Pi_0 \psi_i \psi_j \ddot{\tau}_i + \Pi_1 \lambda_i^4 \psi_i \psi_j \tau_i \right) dx^* = \int_{-1}^{1} \left(2\Delta p^* - \Pi_0 \ddot{h}^* \right) \psi_j dx^*. \tag{2.12}$$

From the orthogonality we obtain the relationship, $\int_{-1}^{1} \psi_i \psi_j dx = 0$ for $i \neq j$. Using this relationship the summation on i is eliminated from the left-hand side and we can re-write Eq. (2.12) as,

$$\Pi_0 \left[\int_{-1}^{1} \psi_j^2 dx^* \right] \ddot{\tau}_j + \Pi_1 \lambda_j^4 \left[\int_{-1}^{1} \psi_j^2 dx^* \right] \tau_j = 2 \int_{-1}^{1} \Delta p^* \psi_j dx^* - \Pi_0 \ddot{h}^* \int_{-1}^{1} \psi_j dx^*. \tag{2.13}$$

15

Let us express the pressure difference by a weighted linear summation of the beam normal functions. This can be done because Δp is a continuous function over the domain of the chord and the beam normal functions are a complete set of orthogonal functions. Therefore, we can express Δp as,

$$\Delta p^* \left(x^*, t^* \right) = \sum_{i=1}^{\infty} Q_i \left(t^* \right) \psi_i \left(x^* \right), \tag{2.14}$$

where the time dependent weighting coefficients Q_i are given by

$$Q_i \left(t^* \right) = \frac{1}{2} \int_{-1}^{1} \Delta p^* \left(x^*, t^* \right) \psi_i \left(x^* \right) dx^*. \tag{2.15}$$

Substituting Eq. (2.14) into the integral containing Δp in Eq. (2.13), we can write the integral as

$$\int_{-1}^{1} \Delta p^* \psi_j dx^* = \sum_{i=1}^{\infty} Q_i \int_{-1}^{1} \psi_i \psi_j dx^* = Q_j \int_{-1}^{1} \psi_j^{\,2} dx^*, \tag{2.16}$$

where we have again utilized the orthogonality relationship of the beam normal functions to eliminate the summation on i. Therefore, each Q_j corresponds to the aerodynamic force with respect to the jth beam mode. Substituting Eq. (2.16) into Eq. (2.13) yields,

$$\Pi_0 \left[\int_{-1}^{1} \psi_j^{\,2} dx^* \right] \ddot{\tau}_j + \Pi_1 \lambda_j^{\,4} \left[\int_{-1}^{1} \psi_j^{\,2} dx^* \right] \tau_j = 2Q_j \left[\int_{-1}^{1} \psi_j^{\,2} dx^* \right] - \Pi_0 \ddot{h}^* \int_{-1}^{1} \psi_j dx^*. \tag{2.17}$$

Finally, we obtain the final form of the governing differential equation by dividing both sides by $\int_{-1}^{1}\psi_j{}^2 dx^*$, resulting in N number of second order ordinary differential equations with the temporal solutions, τ_j, as the independent unknown variables, given as

$$\Pi_0 \ddot{\tau}_j + \Pi_1 \lambda_j{}^4 \tau_j = Q_j^* - q_j \Pi_0 \ddot{h}^*. \tag{2.18}$$

Here $q_j = \int_{-1}^{1}\psi_j dx^* / \int_{-1}^{1}\psi_j{}^2 dx^*$ can be referred to as the Fourier coefficient and is a known constant for each beam mode. Also, Q_j^* is the generalized aerodynamic force with respect to each beam mode, defined as $Q_j^*=2Q_j$. As we will see in Chapter 3, the generalized aerodynamic force introduces nonlocal behavior across all the beam modes because Δp^* is expressed by all the beam modes given in Eq. (2.14).

2.3   Aerodynamic Methodology

We assume the fluid to be inviscid, irrotational, and incompressible such that the potential flow equations govern the flow, for which a velocity potential, Φ, exists and satisfies the Laplace equation,

$$\nabla^2 \Phi = 0. \tag{2.19}$$

We implement the slip boundary condition such that no flow penetrates the surface of the plate. This enforces that the normal velocity of the fluid at the surface of the plate goes to zero, i.e.

$$\left(\nabla \Phi - \mathbf{v}_{rel}\right) \cdot \mathbf{n} = 0, \tag{2.20}$$

where $\mathbf{v}_{rel}$ is the relative motion of the plate, equal to the plate transverse velocity, given as

$$\mathbf{v}_{rel} = \left\{ 0, \frac{\partial v}{\partial t} \right\}.$$

(2.21)

Since the solution to Laplace's equation is linear, its solution can be divided into two parts, such that

$$\Phi = \phi + \phi_\infty,$$

(2.22)

where ϕ is the perturbation velocity potential and ϕ_∞ is the velocity potential due to the uniform free-stream flow given as,

$$\phi_\infty = U_\infty x.$$

(2.23)

The surface normal, $\mathbf{n}$, is defined as,

$$\mathbf{n}(x,t) = \frac{\nabla v}{|\nabla v|} = \frac{1}{|\nabla v|} \left\{ -\frac{\partial v}{\partial x}, 1 \right\},$$

(2.24)

where $\partial v / \partial x$ is the local slope of the surface equal to the local slope of the deformed plate. Substituting Eq. (2.24), Eq. (2.22) and Eq. (2.21) along with the definitions for the velocity potential for the free stream flow into Eq. (2.20) yields,

$$\left\{ \frac{\partial \phi}{\partial x} + U_\infty, \frac{\partial \phi}{\partial y} - \frac{\partial v}{\partial t} \right\} \cdot \frac{1}{|\nabla v|} \left\{ -\frac{\partial v}{\partial x}, 1 \right\} = 0.$$

(2.25)

18

Evaluating the dot product and rearranging terms yields,

$$\frac{\partial \phi}{\partial y} = U_\infty \frac{\partial v}{\partial x} + \frac{\partial v}{\partial t} + \frac{\partial \phi}{\partial x} \frac{\partial v}{\partial x},$$
(2.26)

and by neglecting the higher order term, the vertical perturbation velocity at the surface of the plate is expressed as,

$$\frac{\partial \phi}{\partial y} = U_\infty \frac{\partial v}{\partial x} + \frac{\partial v}{\partial t}.$$
(2.27)

In addition, the solution must satisfy Kelvin's theorem, such that the change in circulation inside the control volume must remain zero, i.e. $d\Gamma/dt=0$. We enforce that far downstream the effects of any perturbation must vanish. Therefore, the gradient of the velocity potential evaluated far downstream must go to zero, i.e. $\lim_{x\to\infty}\nabla\phi=0$. And finally, we must satisfy the Kutta condition, which states that no infinite velocities may exist at the trailing-edge, $x^*=1$, of the plate, i.e. $\nabla\phi(1,t)<\infty$. Following the approach of Theodorsen [19], the perturbation velocity potential is divided into two parts: the noncirculatory part, and the circulatory part. A source/sink sheet is used to model the noncirculatory flow and a vortex sheet is used to model the circulatory flow. Sources, sinks and vortices diminish far downstream, thus satisfying the vanishing condition. The Joukowski conformal mapping is used to map a flat plate in the *xy*-complex plane to a circle in the *XY*-complex plane. We satisfy the slip boundary condition by placing continuous source/sink pairs along the surface of the circle, where the sources are located on the upper half and the sinks are located on the bottom half. The Kutta condition including Kelvin's theorem is satisfied by placing continuous vortex pairs along the positive *X*-axis, where vortex elements are placed outside the

19

circle to infinity and counter vortex elements are placed at their corresponding image positions. When transformed to the xy-plane, the distribution of source/sink pairs will lie along the plate on the x-axis and the vortex pairs will lie on the x-axis spanning from the trailing-edge to infinity. The curvature of the plate is realized by a spatial varying source/sink sheet strength and the vortex sheet represents the wake. It is appropriate to move both sheets to the x-axis since we have enforced small perturbations and assumed a flat wake, allowing us to move the deformed camber line and the wake to lie on the x-axis.

2.3.1 Joukowski's Conformal Mapping

A circle in the XY-plane with radius $b/2$ and its center located at the origin, is transformed into a line or "slit" in the xy-plane where $-b \leq x \leq b$ and $y=0$, by the Joukowski transformation formula, defined as

$$x + \mathrm{i}y = (X + \mathrm{i}Y) + \frac{b^2}{4(X + \mathrm{i}Y)}. \tag{2.28}$$

This transformation maps all the points outside and inside of the circle to a location outside the slit but on different Riemann surfaces [1]. Similarly, all the points on the surface of the circle map directly onto the slit, where again the top and bottom surfaces map to different Riemann surfaces [1]. A diagram showing the Joukowski conformal mapping transformation from the circle in the XY-plane to the slit in the xy-plane is shown in Figure 2.2.
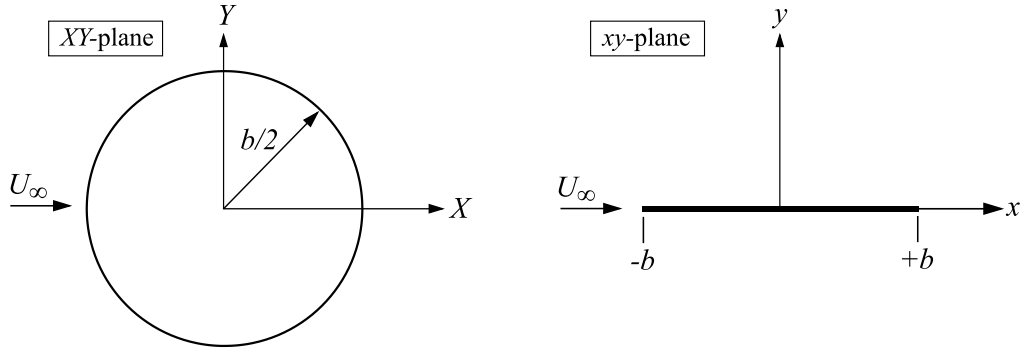
Figure 2.2. Schematic discription of the Joukowski conformal mapping showing the circle in the *XY*-plane (left) and then mapped into a line or "slit" in in the *xy*-plane (right).

There are several important relationships that are used in developing the aerodynamic model. First, we need to define the relation between points on the circle in the *XY*-plane to points in the *xy*-plane. On the surface of the circle, we know that $Y=\sqrt{b^2/4-X^2}$ and substituting into Eq. (2.28) with some manipulation yields,

$$
\begin{aligned}
x+iy &= \left(X+i\sqrt{b^2/4-X^2}\right) + \frac{b^2}{4\left(X+i\sqrt{b^2/4-X^2}\right)} \\
&= \left(X+i\sqrt{b^2/4-X^2}\right) + \frac{b^2}{4\left(X+i\sqrt{b^2/4-X^2}\right)} \frac{\left(X-i\sqrt{b^2/4-X^2}\right)}{\left(X-i\sqrt{b^2/4-X^2}\right)} \\
&= 2X,
\end{aligned}
\tag{2.29}
$$

and by equating reals and imaginaries, we obtain

$$
x=2X, \quad y=0.
\tag{2.30}
$$

21

We also need to define the relation between points on the X-axis in the XY-plane to points on the x-axis in the xy-plane. This is done by setting $Y=0$ in Eq. (2.28) and equating reals and imaginaries, resulting in

$$x = X + \frac{b^2}{4X}, \quad y = 0. \tag{2.31}$$

From this we define the corresponding image position of X, which is located at $b^2/4X$, such that at $X=X_0$ the transformation results in

$$x_0 = X_0 + \frac{b^2}{4X_0}, \quad y_0 = 0, \tag{2.32}$$

for both the position X_0 and for the image position $b_2/4X_0$. This is a useful relationship and will be used in the mathematical model for the circulatory flow.

2.3.2 Noncirculatory Flow

From classical potential aerodynamics, the velocity potential of a source of strength σ located at a location (X_1,Y_1), which lies on the surface of the circle in the XY-plane is given as,

$$\phi_{\text{source}} = \frac{\sigma}{4\pi} \log\left[\left(X - X_1 \right)^2 + \left(Y - Y_1 \right)^2 \right]. \tag{2.33}$$

We place a source of strength $+\sigma$ at (X_1,Y_1) and a sink of strength $-\sigma$ at $(X_1,-Y_1)$, as shown in Figure 2.3. When transformed, both the source and sink will lie at the same x-location on the x-axis, but on different Riemann surfaces. It may appear that the source/sink pair would cancel each other out, however, this is not the case because they lie on different Riemann surfaces. The fluid forced

22

downward by the sources does not go directly into the sinks. It creates another separate streamline

on the second Riemann surface, traveling a long path before coming around and supplying from

above a portion of the fluid required by the sinks [1].
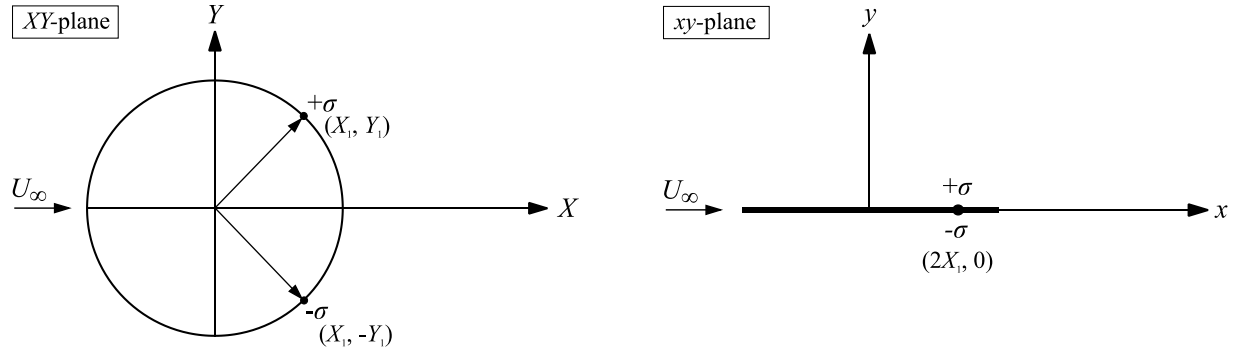
Figure 2.3. Schematic discription showing the source/sink pair on the surface of the circle in the *XY*-plane (left) and then mapped onto the line or "slit" in the *xy*-plane (right).

Therefore, the velocity potential for the source/sink pair can be expressed as,

$$\phi_{\text{source/sink}} = \frac{\sigma}{4\pi} \log\left[\frac{\left(X - X_1\right)^2 + \left(Y - Y_1\right)^2}{\left(X - X_1\right)^2 + \left(Y + Y_1\right)^2}\right]. \tag{2.34}$$

On the surface of a circle, $Y = \sqrt{b^2/4 - X^2}$ and similarly $Y_1 = \sqrt{b^2/4 - X_1^2}$. Substituting this into Eq.

(2.34) yields the velocity potential due to the source/sink pair as a function of X and X_1 only, given

as

23

$$\phi_{\text{source/sink}} = \frac{\sigma}{4\pi}\log\left[\frac{\left(X-X_1\right)^2+\left(\sqrt{b^2/4-X^2}-\sqrt{b^2/4-X_1^{\,2}}\right)^2}{\left(X-X_1\right)^2+\left(\sqrt{b^2/4-X^2}+\sqrt{b^2/4-X_1^{\,2}}\right)^2}\right]. \tag{2.35}$$

Using Eq. (2.30) we transform Eq. (2.35) to the *xy*-plane, which can be expressed as,

$$\phi_{\text{source/sink}} = \frac{\sigma}{4\pi}\log\left[\frac{\left(x-x_1\right)^2+\left(\sqrt{b^2-x^2}-\sqrt{b^2-x_1^{\,2}}\right)^2}{\left(x-x_1\right)^2+\left(\sqrt{b^2-x^2}+\sqrt{b^2-x_1^{\,2}}\right)^2}\right]. \tag{2.36}$$

The flow around the circle is created by placing continuous source/sink pairs along the upper and bottom halves of the circle. Integrating over the chord gives the total velocity potential induced by the source/sink pairs, given by

$$\phi_{nc} = \frac{b}{4\pi}\int_{-1}^{1}\sigma\left(x_1^*,t^*\right)\log\left[\frac{\left(x^*-x_1^*\right)^2+\left(\sqrt{1-x^{*2}}-\sqrt{1-x_1^{*2}}\right)^2}{\left(x^*-x_1^*\right)^2+\left(\sqrt{1-x^{*2}}+\sqrt{1-x_1^{*2}}\right)^2}\right]dx_1^*, \tag{2.37}$$

where we have introduced the non-dimensional coordinates x^* and t^*.

The continuous source/sink sheet strength is obtained by satisfying the slip boundary condition. To do so, we have followed the approach presented by Katz [53]. The velocity potential for a source or sink sheet located on the *x*-axis is defined as,

$$\tilde{\phi}(x^*,y^*,t^*) = \frac{b}{4\pi}\int_{-1}^{1}\tilde{\sigma}\left(x_1^*,t^*\right)\log\left[\left(x^*-x_1^*\right)^2+y^{*2}\right]dx_1^*. \tag{2.38}$$

Therefore, the generated vertical velocity is expressed as,

$$\frac{\partial \tilde{\phi}}{\partial y^*} = \frac{b}{4\pi} \int_{-1}^{1} \tilde{\sigma}\left(x_1^*,t^*\right) \frac{y^*}{\left(x^* - x_1^*\right)^2 + y^{*2}} \, dx_1^*. \tag{2.39}$$

The vertical velocity along the x-axis is obtained by taking the limit of Eq. (2.39) as y goes to zero. However, when $y \to 0$ the integrand is zero except at $x_1^* = x^*$ and thus the integrand only depends on the contribution from this point. Therefore, in the limit of $y \to 0$, $\sigma(x_1^*,t^*)$ can be taken as $\sigma(x^*,t^*)$, and can be removed from the integrand. Furthermore, the limits of integration no longer affect the value of the integral and for convenience will be replaced by $\pm\infty$, such that

$$v\left(x^*,0^\pm,t^*\right) = \frac{\partial \tilde{\phi}(x^*,0^\pm,t^*)}{\partial y^*} = \lim_{y^* \to 0^\pm} \left[\frac{b}{4\pi} \tilde{\sigma}\left(x^*,t^*\right) \int_{-\infty}^{\infty} \frac{y^*}{\left(x^* - x_1^*\right)^2 + y^{*2}} \, dx_1^* \right]. \tag{2.40}$$

Katz [53] evaluates this limit by introducing a new integration variable, defined as $\delta = (x^* - x_1^*)/y$ and obtains the following result.

$$\frac{\partial \tilde{\phi}(x^*,0^\pm,t^*)}{\partial y^*} = \frac{\tilde{\sigma}\left(x^*,t^*\right)}{2} \tag{2.41}$$
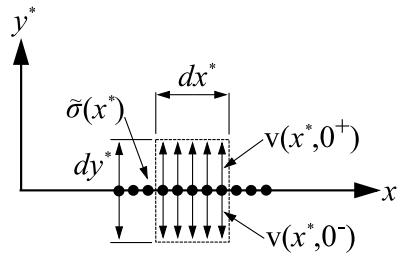
Figure 2.4. Schematic of a differential element of a source sheet and generated veritcal velocity. Adopted from [53].

Therefore, from Eq. (2.41) and Eq. (2.27) we obtain the continuous source/sink sheet strength, given as

$$\sigma\left(x^{*},t^{*}\right)=2\frac{\partial\phi}{\partial y^{*}}=2\left(U_{\infty}\frac{\partial v^{*}}{\partial x^{*}}+bf\frac{\partial v^{*}}{\partial t^{*}}\right).$$ (2.42)

As mentioned earlier, the curvature of the plate is realized by this spatial varying source/sink sheet strength, which satisfies the slip boundary condition.

The pressure acting on the airfoil is determined using Bernoulli's equation for unsteady flow, defined as

$$p+\frac{1}{2}\rho_{f}\left(\nabla\Phi\cdot\nabla\Phi\right)+\rho_{f}\frac{\partial\Phi}{\partial t}=\text{constant},$$ (2.43)

where p is the pressure and the constant of integration is moved to the right-hand side. The Bernoulli's equation is linearized by assuming that the disturbance velocities in the x and y directions are small, such that

$$\begin{aligned}\nabla\Phi\cdot\nabla\Phi &=\left\{\frac{\partial\left(\phi_{\infty}+\phi_{nc}\right)}{\partial x},\frac{\partial\left(\phi_{\infty}+\phi_{nc}\right)}{\partial y}\right\}\cdot\left\{\frac{\partial\left(\phi_{\infty}+\phi_{nc}\right)}{\partial x},\frac{\partial\left(\phi_{\infty}+\phi_{nc}\right)}{\partial y}\right\}\\ &=\left(U_{\infty}+\frac{\partial\phi_{nc}}{\partial x}\right)^{2}+\left(\frac{\partial\phi_{nc}}{\partial y}\right)^{2}\\ &=U_{\infty}^{\ 2}+2U_{\infty}\frac{\partial\phi_{nc}}{\partial x}+\left(\frac{\partial\phi_{nc}}{\partial x}\right)^{2}+\left(\frac{\partial\phi_{nc}}{\partial y}\right)^{2},\end{aligned}$$ (2.44)

and by neglecting higher order terms, we have

$$\nabla \Phi \cdot \nabla \Phi = U_\infty^{\,2} + 2U_\infty \frac{\partial \phi_{nc}}{\partial x}. \tag{2.45}$$

Substituting Eq. (2.45) into Eq. (2.43), we obtain expressions for the pressure acting on the upper and lower surfaces, where potential on the lower surface is the negative of the potential on the upper surface, given as

$$
\begin{aligned}
p_{u,nc}(x,t) &= -\rho_f \left(\frac{1}{2} U_\infty^{\,2} + U_\infty \frac{\partial \phi_{nc}}{\partial x} + \frac{\partial \phi_{nc}}{\partial t} \right) + \text{constant.} \\
p_{l,nc}(x,t) &= -\rho_f \left(\frac{1}{2} U_\infty^{\,2} - U_\infty \frac{\partial \phi_{nc}}{\partial x} - \frac{\partial \phi_{nc}}{\partial t} \right) + \text{constant,}
\end{aligned}
\tag{2.46}
$$

and by taking the difference of the two, the pressure difference due to the noncirculatory flow at a location x^* on the plate is defined as,

$$\Delta p_{nc}\left(x^*, t^*\right) = \left(p_u - p_l\right)_{nc} = 2\rho_f \left(\frac{U_\infty}{b} \frac{\partial \phi_{nc}}{\partial x^*} + f \frac{\partial \phi_{nc}}{\partial t^*} \right). \tag{2.47}$$

2.3.3 Circulatory Flow

From classical potential aerodynamics, the velocity potential of a point vortex of strength $\Delta\Gamma$ located on the X-axis at a location $(X_0, 0)$ in the XY-plane is given as,

$$\phi_{vortex} = -\frac{\Delta\Gamma}{2\pi} \tan^{-1}\left(\frac{Y}{X - X_0} \right). \tag{2.48}$$

We place a counter-vortex element at the corresponding image location $(b^2/4X_0, 0)$ which lies inside the circle. This counter vortex is required to satisfy Kelvin's theorem and to ensure that the

resultant velocity at the surface of the circle is tangent and thus not disrupting the slip boundary condition. The velocity potential for a pair of vortices, one outside the circle at X_0 and the other of opposite strength at the corresponding image position located inside the circle at $b^2/4X_0$, as shown in Figure 2.5, is given as

$$\phi_{\Delta\Gamma} = -\frac{\Delta\Gamma}{2\pi}\left[\tan^{-1}\left(\frac{Y}{X-X_0}\right) - \tan^{-1}\left(\frac{Y}{X-\dfrac{b^2}{4X_0}}\right)\right].$$

(2.49)
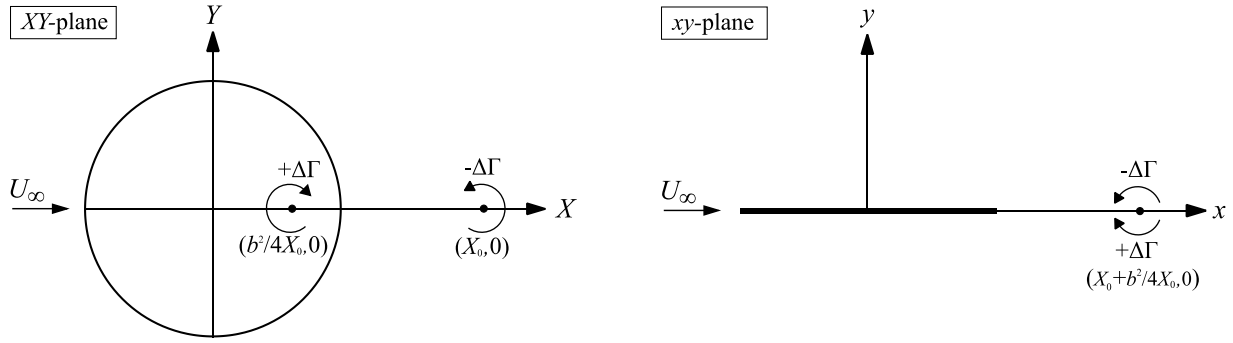
Figure 2.5. Schematic discription showing the vortex pair in the XY-plane (left) and then mapped to the xy-plane (right).

We transform Eq. (2.49) to the xy-plane by introducing the transformation in Eq. (2.31) which can be written as $X_0 = \frac{1}{2}x_0 + \frac{1}{2}\sqrt{x_0^2 - b^2}$ and by acknowledging that $X=x/2$ from Eq. (2.30) and $Y = \frac{1}{2}\sqrt{b^2 - x^2}$ on the surface of the circle, Eq. (2.49) becomes

28

$$\phi_{\Delta\Gamma} = -\frac{\Delta\Gamma}{2\pi}\tan^{-1}\left(\frac{\sqrt{b^2 - x^2}\sqrt{x_0^2 - b^2}}{b^2 - xx_0}\right), \tag{2.50}$$

and introducing non-dimensional coordinates yields,

$$\phi_{\Delta\Gamma} = -\frac{\Delta\Gamma}{2\pi}\tan^{-1}\left(\frac{\sqrt{1 - x^{*2}}\sqrt{x_0^{*2} - 1}}{1 - x^* x_0^*}\right). \tag{2.51}$$

This expression gives the clockwise circulation around the airfoil due to the element $\Delta\Gamma$ at x_0^* [19], which lies in the wake. Helmholtz theorem states that for ideal fluids, under the influence of conservative forces, vortices move with the fluid [54], therefore, we can assume that the vortices propagate downstream at the free stream velocity, such that

$$\frac{\partial x_0}{\partial t} = U_\infty. \tag{2.52}$$

Using Eq. (2.52) along with the chain rule, we can derive the following relation which will be used in calculating the pressure.

$$\frac{\partial \phi_{\Delta\Gamma}}{\partial t} = \frac{\partial \phi_{\Delta\Gamma}}{\partial x_0}\frac{\partial x_0}{\partial t} = \frac{\partial \phi_{\Delta\Gamma}}{\partial x_0}U_\infty \tag{2.53}$$

Considering the linearized unsteady Bernoulli's equation, similar to Eq. (2.47), expressed as

$$\Delta p_{\Delta\Gamma}\left(x^*, t^*\right) = 2\rho_f\left(\frac{U_\infty}{b}\frac{\partial \phi_{\Delta\Gamma}}{\partial x^*} + f\frac{\partial \phi_{\Delta\Gamma}}{\partial t^*}\right), \tag{2.54}$$

29

and using the relation in Eq. (2.53) yields the definition for the pressure difference due to one pair of vortex elements, given as

$$\Delta p_{\Delta\Gamma}\left(x^*,t^*\right) = -\frac{2\rho_f U_\infty}{b}\left(\frac{\partial \phi_{\Delta\Gamma}}{\partial x^*} + \frac{\partial \phi_{\Delta\Gamma}}{\partial x_0^*}\right).$$ (2.55)

The partial derivatives found in Eq. (2.55), evaluate to

$$\frac{\partial \phi_{\Delta\Gamma}}{\partial x^*} = \frac{\Delta\Gamma}{2\pi}\frac{1}{\sqrt{1-x^{*2}}}\frac{\sqrt{x_0^{*2}-1}}{x_0^* - x^*},$$ (2.56)

and

$$\frac{\partial \phi_{\Delta\Gamma}}{\partial x_0^*} = \frac{\Delta\Gamma}{2\pi}\frac{\sqrt{1-x^{*2}}}{\left(x_0^* - x^*\right)\sqrt{x_0^{*2}-1}},$$ (2.57)

where the element -$\Delta\Gamma$ is regarded as moving to the right relative to the plate. Therefore, we can write Eq. (2.55) as,

$$\Delta p_{\Delta\Gamma}\left(x^*,t^*\right) = -\frac{\rho_f U_\infty \Delta\Gamma}{b\pi}\frac{1}{\sqrt{1-x^{*2}}}\frac{x_0^* + x^*}{\sqrt{x_0^{*2}-1}}.$$ (2.58)

We can express the strength of the circulation shed into the wake along the x-axis as,

$$\Delta\Gamma = b\gamma_w\left(x_0^*,t^*\right)dx_0^*,$$ (2.59)

where $\gamma_w(x_0{}^*, t)$ is the circulation per unit length. Therefore, the pressure difference due to the effects of the entire wake, denoted as Δp_c, can be obtained by integrating over the entire wake, given as

$$\Delta p_c\left(x^*, t^*\right) = -\frac{\rho_f U_\infty}{\pi} \frac{1}{\sqrt{1-x^{*2}}} \int_1^\infty \frac{x_0^* + x^*}{\sqrt{x_0^{*2} - 1}} \gamma_w\left(x_0^*, t^*\right) dx_0^*. \tag{2.60}$$

Furthermore, the velocity potential for the circulatory flow due to the entire wake is given as,

$$\phi_c\left(x^*, t^*\right) = -\frac{b}{2\pi} \int_1^\infty \tan^{-1}\left(\frac{\sqrt{1-x^{*2}}\sqrt{x_0^{*2}-1}}{1-x^* x_0^*}\right) \gamma_w\left(x_0^*, t^*\right) dx_0^*. \tag{2.61}$$

Enforcing the Kutta condition we ensure that the flow velocity magnitude at the trailing-edge $x^*=1$ to be finite, such that

$$\frac{\partial\left(\phi_c + \phi_{nc}\right)}{\partial x^*}\bigg|_{x^*=1} = \zeta, \tag{2.62}$$

where ζ is a finite value. The velocity perturbation due to the circulatory flow at the trailing-edge, can be obtained by substituting Eq. (2.59) into Eq. (2.56), given as

$$\frac{\partial\phi_c}{\partial x^*}\bigg|_{x^*=1} = \frac{b}{2\pi}\left[\frac{1}{\sqrt{1-x^{*2}}}\right]_{x^*=1} \int_1^\infty \sqrt{\frac{x_0^*+1}{x_0^*-1}} \gamma_w\left(x_0^*, t^*\right) dx_0^*. \tag{2.63}$$

Note that the evaluation of the diverging term $1/\sqrt{1-x^{*2}}$ will be delayed. Substituting Eq. (2.63) into Eq. (2.62) and multiplying by $\sqrt{1-x^{*2}}$ yields,

$$\frac{b}{2\pi}\int_1^\infty \sqrt{\frac{x_0^*+1}{x_0^*-1}}\ \gamma_w\left(x_0^*,t^*\right)dx_0^* + \left[\sqrt{1-x^{*2}}\ \frac{\partial \phi_{nc}}{\partial x^*}\right]_{x^*=1} = \left[\sqrt{1-x^{*2}}\right]_{x^*=1}\zeta, \tag{2.64}$$

where the finite value ζ goes to zero when evaluated at $x^*=1$. However, the velocity perturbation due to the noncirculatory flow reaches a finite value and is non-zero, due to the existence of $1/\sqrt{1-x^{*2}}$ in the solution. From Eq. (2.64) we define the following function K, given as

$$K\left(t^*\right) = \frac{1}{2\pi}\int_1^\infty \sqrt{\frac{x_0^*+1}{x_0^*-1}}\ \gamma_w\left(x_0^*,t^*\right)dx_0^* = \left[-\frac{\sqrt{1-x^{*2}}}{b}\ \frac{\partial \phi_{nc}}{\partial x^*}\right]_{x^*=1}, \tag{2.65}$$

which is a function of time only. Introducing the function K into the pressure difference in Eq. (2.60) yields,

$$\Delta p_c\left(x^*,t^*\right) = -2\rho_f U_\infty K\ \frac{1}{\sqrt{1-x^{*2}}}\left[\frac{\int_1^\infty \frac{x_0^*+x^*}{\sqrt{x_0^{*2}-1}}\gamma_w\left(x_0^*,t^*\right)dx_0^*}{\int_1^\infty \sqrt{\frac{x_0^*+1}{x_0^*-1}}\ \gamma_w\left(x_0^*,t^*\right)dx_0^*}\right]. \tag{2.66}$$

We assume that the wake vortex sheet strength is harmonic and can be written in terms of the reduced frequency, k, given as

$$\gamma_w\left(x^*,t^*\right) = \bar{\gamma}_w e^{i\left(2\pi t^*-kx^*\right)}, \tag{2.67}$$

where $\bar{\gamma}_w$ is the magnitude. We now introduce Theodorsen's function, defined as

$$C(k) = \frac{\int_1^\infty \dfrac{x_0^*}{\sqrt{x_0^{*2}-1}}\gamma_w\left(x_0^*,t^*\right)dx_0^*}{\int_1^\infty \sqrt{\dfrac{x_0^*+1}{x_0^*-1}}\,\gamma_w\left(x_0^*,t^*\right)dx_0^*} = \frac{\int_1^\infty \dfrac{x_0^*}{\sqrt{x_0^{*2}-1}}e^{-ikx_0^*}dx_0^*}{\int_1^\infty \sqrt{\dfrac{x_0^*+1}{x_0^*-1}}\,e^{-ikx_0^*}\,dx_0^*},$$

(2.68)

which is a complex function of reduced frequency only and this ratio of integrals characterizes the wake. Theodorsen expressed this function in the form of Hankel functions of the second kind, given as,

$$C(k) = \frac{H_1^{(2)}(k)}{H_1^{(2)}(k)+iH_0^{(2)}(k)},$$

(2.69)

where $H_n^{(2)}$ can be written as a combination of Bessel functions of the first and second kinds expressed as, $H_n^{(2)}=J_n-iY_n$. Using the function K and Theodorsen's function we can write the pressure difference due to the circulatory flow as,

$$\Delta p_c\left(x^*,t^*\right) = 2\rho_f U_\infty K \frac{C(k)+x^*\left(1-C(k)\right)}{\sqrt{1-x^{*2}}}.$$

(2.70)

It is evident that the pressure due to the circulatory flow diverges at $x^*=-1$ and $x^*=1$. However, at the trailing-edge, $x^*=1$, the total pressure must be bound due to satisfying the Kutta condition. This indicates that the pressure due to the noncirculatory flow must diverge in the opposite direction at $x^*=1$.

2.3.4 Complete Pressure Difference

The complete perturbation pressure difference, Δp, on the plate is the sum of the pressure difference for the noncirculatory flow given in Eq. (2.47) and the circulatory flow given in Eq. (2.70). This expression is given as

$$\Delta p\left(x^*,t^*\right) = -2\rho_f \left(\frac{U_\infty}{b} \frac{\partial \phi_{nc}}{\partial x^*} + f \frac{\partial \phi_{nc}}{\partial t^*} + \frac{U_\infty}{b} K \frac{C(k) + x^*\left(1-C(k)\right)}{\sqrt{1-x^{*2}}} \right), \tag{2.71}$$

where ϕ_{nc} is given in Eq. (2.37), K is given in Eq. (2.65), and $C(k)$ is given in Eq. (2.69).

CHAPTER 3

TWO-WAY COUPLED AEROELASTIC SOLUTION

3.1   Chebyshev Polynomial Expansion

Chebyshev series is a logical choice for this problem. Chebyshev series are a Fourier cosine expansion with a change in variable [55], however, they have a special property that Fourier series do not have. Chebyshev polynomials have a kind of inherent coordinate-stretching that makes them much better at resolving singularities near the endpoints [55]. This is important since we know that the perturbation pressure difference contains a singularity at the leading-edge, due to assuming an infinitely thin plate. Furthermore, Chebyshev polynomials are a natural choice for non-periodic functions [55], for which the perturbation pressure is not, due to the leading-edge singularity and satisfying the Kutta condition at the trailing-edge.

We express the plate deformation, w^*, in a Chebyshev polynomial expansion of the first kind to aid in the evaluation of the integral for the noncirculatory velocity potential in Eq. (2.37). Chebyshev polynomials are a series of orthogonal polynomials within the interval $-1 \leq x^* \leq 1$ and

with a weight of $1/\sqrt{1-x^{*2}}$. The Chebyshev polynomials are defined by the recurrence relation given as,

$$
\begin{aligned}
T_0\left(x^*\right) &= 1 \\
T_1\left(x^*\right) &= x^* \\
T_{n+1}\left(x^*\right) &= 2x^* T_n\left(x^*\right) - T_{n-1}\left(x^*\right).
\end{aligned}
\tag{3.1}
$$

The first six consecutive Chebyshev polynomials are shown in Figure 3.1.
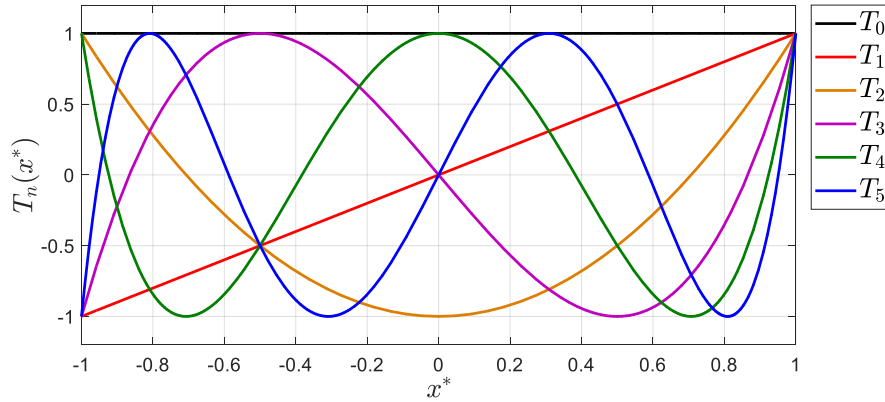
Figure 3.1. Plot of the first six Chebyshev polynomials.

Recall from Eq. (2.8) the plate deformation is written as the sum of the products of the beam normal functions, $\psi_i\left(x^*\right)$, and temporal solutions, $\tau_i\left(t^*\right)$. By expressing each $\psi_i\left(x^*\right)$ in a Chebyshev polynomial expansion, we can express the plate deformation as the following double summation,

$$w^*\left(x^*,t^*\right)=\sum_{i=1}^{\infty}\tau_i\left(t^*\right)\psi_i\left(x^*\right)=\sum_{i=1}^{\infty}\tau_i\left(t^*\right)\left[\sum_{n=0}^{\infty}c_{n,i}T_n\left(x^*\right)\right], \qquad (3.2)$$

where the Chebyshev coefficients, $c_{n,i}$, refer to the ith beam mode determined by,

$$c_{n,i}=\begin{cases}\dfrac{1}{\pi}\displaystyle\int_{-1}^{1}\dfrac{1}{\sqrt{1-x^{*2}}}\psi_i\left(x^*\right)T_0\left(x^*\right)dx^*, & n=0\\[4mm]\dfrac{2}{\pi}\displaystyle\int_{-1}^{1}\dfrac{1}{\sqrt{1-x^{*2}}}\psi_i\left(x^*\right)T_n\left(x^*\right)dx^*, & n>0,\end{cases} \qquad (3.3)$$

which can be tabulated before use, since they are constant.

Since we use an infinite summation series, it is convenient to express any solutions in the form of infinite summations. The following summations of Chebyshev coefficients arise and are used in the solutions of the generalized aerodynamic force, lift, thrust, and power. Summations S_i^1 through S_i^4 are vectors depending on only one set of beam normal functions. Summations S_{ji}^5 through S_{ji}^8 are matrices depending on two independent sets of beam normal functions, where S_{ji}^5, S_{ji}^6 and S_{ji}^7 are symmetric, whereas, S_{ji}^8 is skew symmetric. The indices i and j refer to individual beam modes.

Table 3.1. Summations of Chebyshev coefficients used in the solutions for the generalized aerodynamic force, lift, thrust, and power.

$$S_i^1 = \sum_{n=1}^{\infty} n c_{n,i}$$

$$S_{ji}^5 = \sum_{n=1}^{\infty} n c_{n,i} c_{n,j}$$

$$S_i^2 = \sum_{\substack{n=2 \\ even}}^{\infty} n c_{n,i}$$

$$S_{ji}^6 = \sum_{n=2}^{\infty} \frac{n}{2(n-1)(n+1)} c_{n,i} c_{n,j}$$

$$S_i^3 = \sum_{\substack{n=1 \\ odd}}^{\infty} n c_{n,i}$$

$$S_{ji}^7 = \sum_{n=1}^{\infty} \frac{1}{4(n+1)} \left(c_{n+2,i} c_{n,j} + c_{n,i} c_{n+2,j} \right)$$

$$S_i^4 = \sum_{\substack{n=2 \\ even}}^{\infty} \frac{n}{2} c_{n,i}$$

$$S_{ji}^8 = \sum_{n=1}^{\infty} \left(c_{n+1,i} c_{n,j} - c_{n,i} c_{n+1,j} \right)$$

3.2   Generalized Aerodynamic Force

By expressing the beam normal functions into a Chebyshev polynomial expansion, we are thus expressing the plate deformation in a Chebyshev polynomial expansion. This simplifies the integral for the velocity potential in Eq. (2.37) to an integral of a series of polynomials, of which can be exactly integrated. Recall that the velocity potential for the noncirculatory flow is defined as,

$$\phi_{nc} = \frac{b}{2\pi} \int_{-1}^{1} \sigma\left(x_1^*, t^*\right) \log \left[\frac{\left(x^* - x_1^*\right)^2 + \left(\sqrt{1-x^{*2}} - \sqrt{1-x_1^{*2}}\right)^2}{\left(x^* - x_1^*\right)^2 + \left(\sqrt{1-x^{*2}} + \sqrt{1-x_1^{*2}}\right)^2} \right] dx_1^*, \qquad (2.37)$$

where the continuous source/sink sheet strength, σ, is given in Eq. (2.42). By recalling that $v^* = w^* + h^*$ and by inserting the definition for w^*, given in Eq. (3.2), σ can be expressed as,

$$\sigma\left(x^*,t^*\right) = \left(U_\infty \frac{\partial w^*}{\partial x^*} + bf \frac{\partial w^*}{\partial t^*} + bf \frac{dh^*}{dt^*} \right)$$

$$= U_\infty \sum_{i=1}^{\infty} \tau_i \left[\sum_{n=0}^{\infty} c_{n,i} \frac{dT_n}{dx^*} \right] + bf \sum_{i=1}^{\infty} \frac{d\tau_i}{dt^*} \left[\sum_{n=0}^{\infty} c_{n,i} T_n \right] + bf \frac{dh^*}{dt^*}. \tag{3.4}$$

The velocity potential for the noncirculatory flow can be expressed as a polynomial containing Chebyshev coefficients, corresponding to the ith beam mode, i.e. $\phi_{nc,i}(x^*,t^*,c_{n,i})$. Since σ is expressed in a series of polynomials, the integration can be evaluated term by term. All parameters except for x_1^* are constant in the integration, including the Chebyshev coefficients. Therefore, to obtain the solution we only need to evaluate the integral at all the powers of x_1^*. Table A.1 in Appendix A shows the solutions to the integral in Eq. (2.37) for the first 6 consecutive powers of x_1^*. It should be noted that when evaluating the integral, the Cauchy principle value should be used [53].

Furthermore, the pressure difference can also be expressed as a polynomial containing Chebyshev coefficients with respect to each beam mode. We can write Eq. (2.71) as,

$$\Delta p_i\left(x^*,t^*\right) = -2\rho_f \left(\frac{U_\infty}{b} \sum_{n=0}^{\infty} \frac{\partial \phi_{nc,i}}{\partial x^*} + f \sum_{n=0}^{\infty} \frac{\partial \phi_{nc,i}}{\partial t^*} + \frac{U_\infty}{b} \sum_{n=0}^{\infty} K_i \frac{C(k) + x^*\left(1 - C(k)\right)}{\sqrt{1 - x^{*2}}} \right), \tag{3.5}$$

where K_i is the function defined in Eq. (2.65) with respect to each beam mode. We included summations on n in front of $\phi_{nc,i}$ and K_i to indicate that these terms are expressed in an infinite series of Chebyshev coefficients. The complete pressure difference is the sum of all i^{th} terms, given as,

$$\Delta p\left(x^*,t^*\right) = \sum_{i=1}^{\infty} \Delta p_i\left(x^*,t^*\right). \tag{3.6}$$

Substituting Eq. (3.6) into Eq. (2.15), we can write the generalized aerodynamic force in the following index notation form,

$$Q_j = \int_{-1}^{1} \Delta p^* \psi_j dx^* = -\sum_{i=1}^{\infty} \left(\kappa_{ji}^{\mathrm{m}} \ddot{\tau}_i + \kappa_{ji}^{\mathrm{c}} \dot{\tau}_i + \kappa_{ji}^{\mathrm{k}} \tau_i + \mu_j \ddot{h}^* + \eta_j \dot{h}^* \right), \qquad (3.7)$$

where the indices i and j refer to individual beam modes and arise due to Δp being expressed in one set of normal functions, indicated by subscript i, and then multiplied by another set of normal functions, indicated by subscript j, which was done to utilize the orthogonality properties to derive the equation of motion. This introduces nonlocal behavior in the general aerodynamic force. The κ_{ji}^{m}, κ_{ji}^{c} and κ_{ji}^{k} terms are related to the aerodynamic loading due to the plate curvature, where the superscripts m, c, and k denote inertia, damping and stiffness, respectively. The terms μ and η are from the inertia load due to the imposed plunge acceleration and velocity, respectively. The normalized aerodynamic force terms κ_{ji}^{m}, κ_{ji}^{c}, κ_{ji}^{k}, μ, and η can be expressed in closed-form as a function of Chebyshev coefficients, given as

$$\kappa_{ji}^{\mathrm{m}} = \frac{k^2}{4\pi} \left(c_{0,i} c_{0,j} + \frac{1}{8} c_{1,i} c_{1,j} - \frac{1}{2} \left(c_{0,i} c_{2,j} + c_{2,i} c_{0,j} \right) + S_{ji}^6 - S_{ji}^7 \right) \qquad (3.8a)$$

$$\kappa_{ji}^{\mathrm{c}} = \frac{k}{4} \left(C(k) \left(2c_{0,i} + c_{1,i} \right) \left(2c_{0,j} - c_{1,j} \right) + c_{1,i} \left(2c_{0,j} + c_{1,j} \right) + 2 S_{ji}^8 \right) \qquad (3.8b)$$

$$\kappa_{ji}^{\mathrm{k}} = \pi \left(C(k)(2c_{0,j} - c_{1,j}) S_i^1 + c_{1,j} S_i^1 - S_{ji}^5 \right) \qquad (3.8c)$$

$$\mu_j = \frac{k^2}{8\pi} \left(2c_{0,j} - c_{2,j} \right) \qquad (3.8d)$$

$$\eta_j = \frac{k}{2} C(k) \left(2c_{0,j} - c_{1,j} \right), \qquad (3.8e)$$

where the Chebyshev summations, S^n's, are defined in Table 3.1. As you can see, the aerodynamic terms only depend on the reduced frequency, k. The terms κ_{ji}^{m}, κ_{ji}^{c} and κ_{ji}^{k} are fully populated matrices, where the inertia term, κ_{ji}^{m}, is symmetric while the damping term, κ_{ji}^{c}, and stiffness term, κ_{ji}^{k}, are non-symmetric.

3.3   Solution

The complete two-way coupled aeroelastic equation of motion can be written by substituting the solution to the generalized aerodynamic force given in Eq. (3.7) into Eq. (2.18). Grouping the temporal solution derivatives to the left-hand side and keeping the forcing terms on the right-hand side yields,

$$\sum_{i=1}^{\infty}\left(\Pi_0\delta_{ji}+\kappa_{ji}^{\text{m}}\right)\ddot{\tau}_i+\left(\kappa_{ji}^{\text{c}}\right)\dot{\tau}_i+\left(\Pi_1\lambda_j^{4}\delta_{ji}+\kappa_{ji}^{\text{k}}\right)\tau_i=-\left(q_j\Pi_0+\mu_j\right)\ddot{h}^{*}-\eta_j\dot{h}^{*}. \qquad (3.9)$$

Eq. (3.9) represents the jth equation, which is made nonlocal by index i. It is apparent that κ_{ji}^{m}, κ_{ji}^{c} and κ_{ji}^{k} are the aeroelastic inertia, damping, and stiffness, respectively, with respect to the plate deformation. Additionally, the terms μ_j and η_j are the aeroelastic inertia and damping, respectively, with respect to the plunging excitation. This should be of no surprise, for it is well known that aeroelastic systems introduce added mass, aeroelastic damping, and stiffness to the equation of motion. Eq. (3.9) clearly distinguishes the aeroelastic contribution between the plate and excitation dynamics. The equation of motion in Eq. (3.9) can be written in matrix form given as,

$$
\begin{bmatrix}
\Pi_0 + \kappa_{11}^m & \kappa_{12}^m & \cdots & \kappa_{1N}^m \\
\kappa_{21}^m & \Pi_0 + \kappa_{22}^m & \cdots & \kappa_{2N}^m \\
\vdots & \vdots & \ddots & \vdots \\
\kappa_{N1}^m & \kappa_{N2}^m & \cdots & \Pi_0 + \kappa_{NN}^m
\end{bmatrix}
\begin{Bmatrix}
\ddot{\tau}_1 \\ \ddot{\tau}_2 \\ \vdots \\ \ddot{\tau}_N
\end{Bmatrix}
+
\begin{bmatrix}
\kappa_{11}^c & \kappa_{12}^c & \cdots & \kappa_{1N}^c \\
\kappa_{21}^c & \kappa_{22}^c & \cdots & \kappa_{2N}^c \\
\vdots & \vdots & \ddots & \vdots \\
\kappa_{N1}^c & \kappa_{N2}^c & \cdots & \kappa_{NN}^c
\end{bmatrix}
\begin{Bmatrix}
\dot{\tau}_1 \\ \dot{\tau}_2 \\ \vdots \\ \dot{\tau}_N
\end{Bmatrix}
$$
$$
+
\begin{bmatrix}
\Pi_1 \lambda_1^{\,4} + \kappa_{11}^k & \kappa_{12}^k & \cdots & \kappa_{1N}^k \\
\kappa_{21}^k & \Pi_1 \lambda_2^{\,4} + \kappa_{22}^k & \cdots & \kappa_{2N}^k \\
\vdots & \vdots & \ddots & \vdots \\
\kappa_{N1}^k & \kappa_{N2}^k & \cdots & \Pi_1 \lambda_N^{\,4} + \kappa_{NN}^k
\end{bmatrix}
\begin{Bmatrix}
\tau_1 \\ \tau_2 \\ \vdots \\ \tau_N
\end{Bmatrix}
=
\begin{Bmatrix}
-\left(q_1 \Pi_0 + \mu_1\right)\ddot{h}^* - \eta_1 \dot{h}^* \\
-\left(q_2 \Pi_0 + \mu_2\right)\ddot{h}^* - \eta_2 \dot{h}^* \\
\vdots \\
-\left(q_N \Pi_0 + \mu_N\right)\ddot{h}^* - \eta_N \dot{h}^*
\end{Bmatrix},
\tag{3.10}
$$

where N is the highest mode considered. Furthermore, we can write Eq. (3.10) in the following abbreviated matrix from,

$$
[\mathbf{M}]\{\ddot{\boldsymbol{\tau}}\} + [\mathbf{C}]\{\dot{\boldsymbol{\tau}}\} + [\mathbf{K}]\{\boldsymbol{\tau}\} = \{\mathbf{F}\},
\tag{3.11}
$$

where the matrices $\mathbf{M}$, $\mathbf{C}$, and $\mathbf{K}$ are the mass, damping, and stiffness matrices, respectively, and the vector $\mathbf{F}$ is the force vector.

3.3.1   Homogeneous Solution

Taking the homogenous state of Eq. (3.11), we obtain

$$
[\mathbf{M}]\{\ddot{\boldsymbol{\tau}}\} + [\mathbf{C}]\{\dot{\boldsymbol{\tau}}\} + [\mathbf{K}]\{\boldsymbol{\tau}\} = \mathbf{0}.
\tag{3.12}
$$

Stability or often referred to as flutter analysis can be performed on this aeroelastic system. At the stability boundary, the motion is harmonic and takes the form,

$$
\boldsymbol{\tau} = \bar{\boldsymbol{\tau}} e^{st},
\tag{3.13}
$$

where $\bar{\tau}$ is the modal amplitude and s is equal to $\delta+ik$, where δ and k are the reduced damping and reduced frequency, respectively. Substituting Eq. (3.13) into Eq. (3.12) yields the following,

$$\left[s^2\mathbf{M}(s) + s\mathbf{C}(s) + \mathbf{K}(s)\right]\bar{\tau} = 0, \qquad (3.14)$$

where matrices $\mathbf{M}$, $\mathbf{C}$ and $\mathbf{K}$ depend on the variable s. In order for the system to have a non-trivial solution, the determinant of the bracketed terms must be zero. To determine the pole locations, the system in Eq. (3.12) is transformed into state-space form given as,

$$\dot{\mathbf{x}} = \mathbf{A}\mathbf{x}, \qquad (3.15)$$

where the state vector $\mathbf{x}$ is defined as,

$$\mathbf{x} = \left\{\begin{matrix} \boldsymbol{\tau} \\ \dot{\boldsymbol{\tau}} \end{matrix}\right\}, \qquad (3.16)$$

and the system matrix $\mathbf{A}$ can be written as,

$$\mathbf{A} = \begin{bmatrix} \mathbf{0} & \mathbf{I} \\ -\mathbf{M}^{-1}\mathbf{K} & -\mathbf{M}^{-1}\mathbf{C} \end{bmatrix}. \qquad (3.17)$$

Taking the Laplace Transform of Eq. (3.15) yields,

$$s\mathbf{x}(s) = \mathbf{A}(s)\mathbf{x}(s), \qquad (3.18)$$

and rearranging terms gives,

$$[s\mathbf{I} - \mathbf{A}(s)]\mathbf{x}(s) = \mathbf{0}. \tag{3.19}$$

Therefore, the pole locations are determined by solving the following equation.

$$|s\mathbf{I} - \mathbf{A}(s)| = \mathbf{0} \tag{3.20}$$

Because $\mathbf{M}$, $\mathbf{C}$ and $\mathbf{K}$ depend on s, the system matrix $\mathbf{A}$ also depends on s, and therefore, an iterative method is required to solve Eq. (3.20).

3.3.2 Forced Vibration Solution

We assume that the plate response due to the imposed harmonic plunging motion given in Eq. (2.3) is also harmonic, such that the jth temporal solution can be expressed as,

$$\tau_j\left(t^*\right) = Z_j e^{\mathrm{i}\varphi_j} e^{\mathrm{i}2\pi t^*}, \tag{3.21}$$

where Z_j and φ_j are the magnitude and phase lag, respectively, with respect to the jth solution. Substituting Eq. (3.21) into Eq. (3.11) and evaluating the time derivatives of τ_j yields,

$$\left[A_{ji}\right]\left\{Z_j e^{\mathrm{i}\varphi_j}\right\} = \left\{F_j\right\}, \tag{3.22}$$

where A_{ji} is equal to $-4\pi^2 M_{ji} + \mathrm{i}2\pi C_{ji} + K_{ji}$ and F_j is equal to $-(q_j\Pi_0 + \mu_j)\ddot{h}^* - \eta_j\dot{h}^*$. Since A_{ji} and F_j are known constants, Eq. (3.22) can be solved analytically and an iterative solver is not required. This system of linear equations can be solved using Cramer's rule. Expanding Eq. (3.22) into matrix form yields,

$$
\begin{bmatrix} A_{11} & A_{12} & \cdots & A_{1N} \\ A_{21} & A_{22} & \cdots & A_{2N} \\ \vdots & \vdots & \ddots & \vdots \\ A_{N1} & A_{N2} & \cdots & A_{NN} \end{bmatrix} \begin{Bmatrix} Z_1 e^{i\varphi_1} \\ Z_2 e^{i\varphi_2} \\ \vdots \\ Z_N e^{i\varphi_N} \end{Bmatrix} = \begin{Bmatrix} F_1 \\ F_2 \\ \vdots \\ F_N \end{Bmatrix},
$$

(3.23)

where N is the highest mode considered in the solution. We define a coefficient matrix for each jth unknown by substituting the force vector, **F**, in the jth column in the system matrix, **A**, as shown below,

$$
\mathbf{D}_1 = \begin{bmatrix} F_1 & A_{12} & \cdots & A_{1N} \\ F_2 & A_{22} & \cdots & A_{2N} \\ \vdots & \vdots & \ddots & \vdots \\ F_N & A_{N2} & \cdots & A_{NN} \end{bmatrix}, \quad \mathbf{D}_2 = \begin{bmatrix} A_{11} & F_1 & \cdots & A_{1N} \\ A_{21} & F_2 & \cdots & A_{2N} \\ \vdots & \vdots & \ddots & \vdots \\ A_{N1} & F_N & \cdots & A_{NN} \end{bmatrix},
$$

where the Nth coefficient matrix is defined as,

$$
\mathbf{D}_N = \begin{bmatrix} A_{11} & A_{12} & \cdots & F_1 \\ A_{21} & A_{22} & \cdots & F_2 \\ \vdots & \vdots & \ddots & \vdots \\ A_{N1} & A_{N2} & \cdots & F_N \end{bmatrix}.
$$

The solution for each $Z_j e^{i\varphi_j}$ is determined by dividing the determinate of the coefficient matrix by the determinant of the system matrix, i.e.

$$
Z_j e^{i\varphi_j} = \frac{|\mathbf{D}_j|}{|\mathbf{A}|}.
$$

(3.24)

From Eq. (2.8) the solution for the plate deformation is given as,

$$w\left(x^{*},t^{*}\right)=\sum_{j=1}^{N}\psi_{j}\left(x^{*}\right)\tau_{j}\left(t^{*}\right)=\Re\left\{\sum_{j=1}^{N}\psi_{j}\left(x^{*}\right)Z_{j}e^{\mathrm{i}\varphi_{j}}e^{\mathrm{i}2\pi t^{*}}\right\},\tag{3.25}$$

where the real part of the complex value solution is taken. We note that the exact beam normal function is used in Eq. (3.25), preserving the exact solution to the structural model. If only *n* number of Chebyshev polynomials are considered, then there exists a truncation error only in the aerodynamic model to describe the aerodynamic loading. However, if *n* is sufficiently large enough, then this truncation error is negligible.

3.3.3 Single-mode Solution

For the case of flapping wings, the flapping frequency of insects and birds is typically much less than the first natural structural frequency in the spanwise and chordwise directions [2]. Therefore, it is possible that the first mode dominates the aeroelastic response. Considering only the first mode, the system nonlocal behavior is eliminated and the motion is described by a single equation. Substituting Eq. (3.7) into Eq. (2.18) yields the local aeroelastic model, given as

$$\left(\Pi_{0}+\kappa_{11}^{\mathrm{m}}\right)\ddot{\tau}_{1}+\left(\kappa_{11}^{\mathrm{c}}\right)\dot{\tau}_{1}+\left(\Pi_{1}\lambda_{1}^{4}+\kappa_{11}^{\mathrm{k}}\right)\tau_{1}=-\left(q_{1}\Pi_{0}+\mu_{1}\right)\ddot{h}^{*}-\eta_{1}\dot{h}^{*},\tag{3.26}$$

where h^{*} is the normalized harmonic plunging excitation motion, originally defined in Eq. (2.3) in dimensional form. It is important to note that Eq. (3.26) still accounts for the coupling between the structure and fluid. The nondimensional form is given as,

$$h^{*}\left(t^{*}\right)=h_{a}^{*}\left(e^{\mathrm{i}2\pi t^{*}}-1\right),\tag{3.27}$$

where $h_a{}^*=h_a/b$. The response of the plate is also harmonic, such that $\tau_1(t^*)=Z_1 e^{i\varphi_1} e^{i2\pi t^*}$, where Z_1 is the magnitude and φ_1 is the phase lag. Evaluating the time derivatives gives,

$$-4\pi^2\left(\Pi_0+\kappa_{11}^{\mathrm{m}}\right)Z_1 e^{i\varphi_1} e^{i2\pi t^*} + 2\pi i\left(\kappa_{11}^{\mathrm{c}}\right)Z_1 e^{i\varphi_1} e^{i2\pi t^*} + \left(\Pi_1\lambda_1^{\,4}+\kappa_{11}^{\mathrm{k}}\right)Z_1 e^{i\varphi_1} e^{i2\pi t^*}$$
$$= 4\pi^2 h_a^*\left(q_1\Pi_0+\mu_1\right)e^{i2\pi t^*} - 2\pi i h_a^* \eta_1 e^{i2\pi t^*}, \tag{3.28}$$

and solving for $Z_1 e^{i\varphi_1}$ yields,

$$Z_1 e^{i\varphi_1} = \frac{4\pi^2 h_a^*\left(q_1\Pi_0+\mu_1\right)-i2\pi h_a^* \eta_1}{-4\pi^2\left(\Pi_0+\kappa_{11}^{\mathrm{m}}\right)+i2\pi\kappa_{11}^{\mathrm{c}}+\Pi_1\lambda_1^{\,4}+\kappa_{11}^{\mathrm{k}}}. \tag{3.29}$$

We introduce the Strouhal number, $St=2h_a f/U_\infty$, a nondimensional parameter that compares the oscillatory flow velocity scale $2h_a f$ to the freestream velocity scale U_∞. Using the Strouhal number we obtain the relations $h_a^*\Pi_0 = \rho^* h_s^* k St/\pi$ and $h_a^* k = \pi St$. Knowing that the beam first natural frequency in vacuum is given as,

$$f_1 = \frac{\lambda_1}{2\pi}\sqrt{\frac{EI}{\rho_s A}}, \tag{3.30}$$

we can define a frequency ratio, which gives the ratio between the driving frequency and the first natural frequency, which can be expressed as

$$f_1^* = \frac{f}{f_1} = \sqrt{\frac{\Pi_0}{\Pi_1}\frac{4\pi^2}{\lambda_1^{\,4}}}. \tag{3.31}$$

47

As we will see in Section 4.3, the frequency ratio can be useful to identify when the single-mode solution can be used with minimal error. Rearranging terms in Eq. (3.29), substituting the definitions for μ and η, and utilizing the Strouhal number and frequency ratio, we can re-write Eq. (3.29) as,

$$Z_1 e^{i\varphi_1} = \frac{\pi^2 St\left[k\left(\frac{4}{\pi}\rho^* h_s^* q_1 + \frac{1}{2}(2c_0 - c_2)\right) - iC(k)(2c_0 - c_1)\right]}{4\pi^2\Pi_0\left(\frac{1}{f_1^{*2}} - 1\right) - 4\pi^2\kappa_{11}^m + i2\pi\kappa_{11}^c + \kappa_{11}^k}. \tag{3.32}$$

From Eq. (2.8) the plate deformation is expressed as,

$$w\left(x^*, t^*\right) = \psi_1\left(x^*\right)\tau_1\left(t^*\right) = \Re\left\{\psi_1\left(x^*\right)Z_1 e^{i\varphi_1} e^{i2\pi t^*}\right\}, \tag{3.33}$$

where we have taken the real part of the complex valued solution. In summary, Eq. (3.33) is a notable single equation that describes the two-way coupling aeroelastic response of chordwise flexibility of flapping wings in forward flight that includes the effect of curvature in the aerodynamic loading.

3.4 Lift

To determine the lift force, we consider a differential element on the plate, as shown in Figure 3.2. The differential lift force, dL, is equal to the force component perpendicular to the free-stream flow, given as,

$$dL = \left(\Delta p dx\right)\cos\left(\frac{\partial v}{\partial x}\right). \tag{3.34}$$
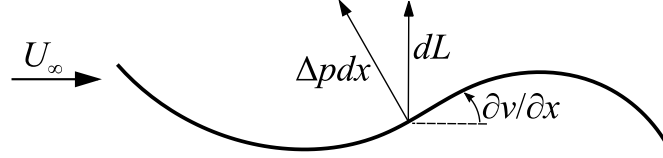
Figure 3.2. Schematic discription for deriving the lift force.

Recalling that $\partial v/\partial x \ll 1$, from the small perturbation assumption, we have $dL=\Delta pdx$. Therefore, the total lift force per unit span, L', can be obtained by integrating the net pressure force along the chord, given as

$$L'\left(t^*\right)=b\int_{-1}^{1}\Delta p\left(x^*,t^*\right)dx^*=b\int_{-1}^{1}\left(\Delta p_{nc}+\Delta p_c\right)dx^*=L_{nc}{}'+L_c{}'. \qquad (3.35)$$

It is convenient to separate the total lift into noncirculatory and circulatory components, as we have shown in Eq. (3.35). Introducing the Chebyshev expansion for the plate deformation given in Eq. (3.2), and evaluating Eq. (3.35) yields the lift force due to each beam mode expressed in closed-form described in Chebyshev coefficients, given as

$$\begin{aligned} L_i'\left(t^*\right)=\Re\Bigg\{ &-\pi\rho_f b^2\left[b\ddot{h}^*+\frac{1}{2}b\left(2c_{0,i}-c_{2,i}\right)\ddot{\tau}_i+U_\infty c_{1,i}\dot{\tau}_i\right]\\ &-2\pi\rho_f U_\infty bC(k)\left[b\dot{h}^*+\frac{1}{2}b\left(2c_{0,i}+c_{1,i}\right)\dot{\tau}_i+US_i^1\tau_i\right]\Bigg\}, \end{aligned} \qquad (3.36)$$

where $\Re$ is the real part of the complex valued solution. The first part is due to the noncirculatory flow and second from the circulatory flow. Here the subscript i refers to the ith beam mode and the total lift is the summation of the lift force due to all the beam modes, given as

$$L'\left(t^*\right) = \sum_{i=1}^{\infty} L_i'\left(t^*\right). \tag{3.37}$$

The classical solution for the lift force for a rigid airfoil undergoing rigid body motion, derived by Theodorsen [19] can be recovered from the lift expression in Eq. (3.36). To model a rigid airfoil, we only need to consider one structural mode, such that $i=1$, where only the Chebyshev coefficients c_0 and c_1 are nonzero. This reduces Eq. (3.36) to

$$\begin{aligned} L'_{rigid}\left(t^*\right) = \Re\Big\{ &-\pi\rho_f b^2\left[b\ddot{h}^* + bc_0\ddot{\tau} + U_\infty c_1\dot{\tau}\right] \\ &-2\pi\rho_f U_\infty bC(k)\left[b\dot{h}^* + \frac{1}{2}b\left(2c_0 + c_1\right)\dot{\tau} + Uc_1\tau\right]\Big\}. \end{aligned} \tag{3.38}$$

Theodorsen [19] allows the rigid airfoil to plunge and pitch, where the location of the elastic axis is denoted by the letter a, which is measured from the y-axis positive in the x-direction. To model this with the current model, we set $c_1=1$ and $c_0=-a$. Substituting this into Eq. (3.38) yields

$$L'_{rigid}\left(t^*\right) = \Re\left\{-\pi\rho_f b^2\left[b\ddot{h}^* - ba\ddot{\tau} + U_\infty\dot{\tau}\right] - 2\pi\rho_f U_\infty bC(k)\left[b\dot{h}^* + b\left(\frac{1}{2} - a\right)\dot{\tau} + U\tau\right]\right\}. \tag{3.39}$$

By realizing that the temporal solution, τ, now represents the angle of attack, α, Eq. (3.39) is equivalent to the lift force derived by Theodorsen [19] for a rigid airfoil undergoing rigid body motion.

3.5   Thrust

The total forward thrust per unit span, T', generated by the plunging and deforming plate is a combination of the thrust due to the leading-edge suction, T'_{LES}, and the thrust due to the

pressure difference, T'_p, such that $T'=T'_{LES}+T'_p$. The leading-edge suction, S, is generated by the vorticity at the leading-edge. By evaluating Eq. (2.62) at $x^*=-1$ we know that the velocity at the leading-edge goes to infinity. This is mathematically correct, however, not physically possible. This is a consequence of using an infinitely thin flat plate with a sharp leading-edge in the aerodynamic model. When the plate is at an angle of attack, the stagnation point moves from the leading-edge to some other location on the plate, as shown in Figure 3.3. This requires the flow to turn exactly 180° resulting in an infinite acceleration and hence an infinite velocity.
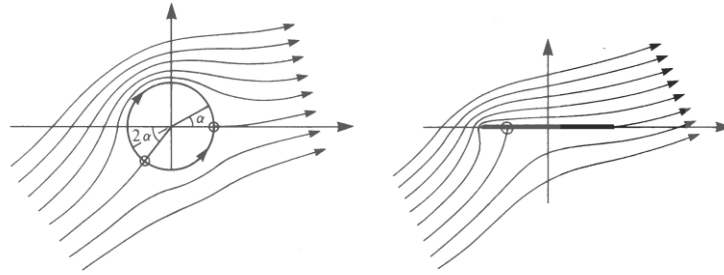
Figure 3.3. Schematic description of the streamlines for a circle in the *XY*-plane (left) to a flat plate in the *xy*-plane (right). Adopted from [53].

It was shown by Karman and Burgers [56] that the leading-edge suction approaches infinity in a functional form of $1/\sqrt{1+x^*}$. Using this, the leading-edge velocity may be written as,

$$\frac{\partial}{\partial x^*}\left(\phi_c+\phi_{nc}\right)_{x^*=-1} = \frac{S}{\sqrt{1+x^*}}. \qquad (3.40)$$

Therefore, an expression for *S* can be derived in terms of the functions *K* and *C(k)*, given as

$$S = \frac{\sqrt{2}}{2} K\left(2C(k)-1\right)+\left[\frac{\sqrt{1+x^*}}{b}\frac{\partial\phi_{nc}}{\partial x^*}\right]_{x^*=-1}. \tag{3.41}$$

The thrust due to the leading-edge suction is defined as $T_{LES}=\pi\rho_f S^2$ and substituting the value for S we obtain the following expression for the leading-edge suction, given as

$$T'_{LES} = \pi\rho_f b \left(\frac{\sqrt{2}}{2} K\left(2C(k)-1\right)+\left[\frac{\sqrt{1+x^*}}{b}\frac{\partial\phi_{nc}}{\partial x^*}\right]_{x^*=-1}\right)^2. \tag{3.42}$$

Introducing the Chebyshev expansion for the plate deformation, given in Eq. (3.2), and evaluating Eq. (3.42), the thrust due to the leading-edge suction can be expressed in closed-form described in Chebyshev coefficients given as,

$$\begin{aligned}
T'_{LES,i}\left(t^*\right) = \Re\Bigg\{\pi\rho_f b\Bigg[&2U_\infty^2\left(C(k)S_i^1-2S_i^4\right)^2\tau_i^2+2b^2C(k)\left(C(k)\left(2c_{0,i}+c_{1,i}\right)-c_{1,i}\right)\dot{\tau}_i\dot{h}^* \\
&+\frac{1}{2}b^2\left(c_{1,i}-C(k)\left(2c_{0,i}+c_{1,i}\right)\right)^2\dot{\tau}_i^2+4U_\infty bC(k)\left(C(k)S_i^1-2S_i^4\right)\tau_i\dot{h}^* \\
&+2U_\infty b\left(C(k)\left(2c_{0,i}+c_{1,i}\right)-c_{1,i}\right)\left(C(k)S_i^1-2S_i^4\right)\tau_i\dot{\tau}_i+2b^2C(k)^2\dot{h}^{*2}\Bigg]\Bigg\},
\end{aligned} \tag{3.43}$$

where the subscript i refers to the ith beam mode and the real part of the complex valued solution is taken.

To determine the thrust due to the pressure, we consider a differential element on the plate, as shown in Figure 3.4. The differential thrust force due to the pressure is equal to the force component tangent to the beam, given as,

$$dT_p = \left(\Delta p dx\right)\tan\left(\frac{\partial v}{\partial x}\right). \tag{3.44}$$

52
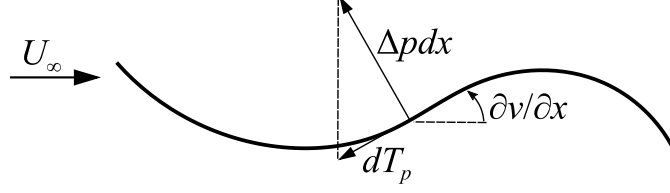
Figure 3.4. Schematic discription for deriving the thrust force due to the pressure difference.

Recalling that $\partial v/\partial x \ll 1$, we have $dT_p = \Delta p dx (\partial v/\partial x)$. Therefore, the thrust force due to the pressure can be obtained by integrating the pressure force multiplied by the local slope over the chord, given as

$$T_p'\left(t^*\right) = b\int_{-1}^{1} \Delta p\left(x^*,t^*\right)\frac{\partial v\left(x^*,t^*\right)}{\partial x^*}dx^* . \tag{3.45}$$

Introducing the Chebyshev expansion for the plate deformation given in Eq. (3.2), and evaluating Eq. (3.45) the thrust due to pressure can be expressed in closed-form described in Chebyshev coefficients, given as

$$\begin{aligned} T_{p,i}'\left(t^*\right) = \Re\Big\{ &-\pi\rho_f b\Big[2U_\infty^2\left(4S_i^4 S_i^4 + C(k)\left(S_i^3 - S_i^2\right)S_i^1\right)\tau_i^2 \\ &+U_\infty b\left(2S_{ii}^5 + \left(C(k)\left(2c_{0,i}+c_{1,i}\right)-c_{1,i}\right)\left(S_i^3 - S_i^2\right)\right)\tau_i\dot{\tau}_i \\ &+2U_\infty bC(k)\left(S_i^3 - S_i^2\right)\tau_i\dot{h}^* + b^2 c_{1,i}\tau_i\ddot{h}^* + b^2 c_{0,i}c_{1,i}\tau_i\ddot{\tau}_i \Big]\Big\}, \end{aligned} \tag{3.46}$$

where the subscript i refers to the ith beam mode and again we take the real part of the complex valued solution.

The total thrust is the sum of the thrust due to the leading-edge suction and the thrust due to pressure summed over all the beam modes, given as

$$T'\left(t^{*}\right)=\sum_{i=1}^{\infty}T'_{p,i}\left(t^{*}\right)+T'_{LES,i}\left(t^{*}\right). \tag{3.47}$$

3.6   Power

In order to maintain the prescribed plunging motion, an external force equal and opposite to the pressure force must be applied. On a differential element dx the external force is $\Delta p dx$, acting in the positive y-direction. Therefore, the power per unit span, P', required to drive the oscillation is defined as the time rate of work done by this external force, i.e. the external force multiplied by the total plate velocity, given as

$$P'\left(t^{*}\right)=b^{2}\int_{-1}^{1}\Delta p\left(x^{*},t^{*}\right)\frac{\partial v\left(x^{*},t^{*}\right)}{\partial t^{*}}dx^{*}. \tag{3.48}$$

Since v is the total plate displacement, this definition of the power not only includes the imposed plunging excitation but the plate deformations as well. Introducing the Chebyshev expansion for the plate deformation given in Eq. (3.2), and evaluating Eq. (3.48) the power can be expressed in closed-form described in Chebyshev coefficients, given as

$$P_i'(t^*) = \Re\left\{-\pi\rho_f b\left[U_\infty^2 b\left(c_{1,i}S_i^1 - S_{ii}^5 + C(k)\left(2c_{0,i} - c_{1,i}\right)S_i^1\right)\tau_i\dot{\tau}_i\right.\right.$$

$$+2U_\infty^2 bC(k)S_i^1\tau_i\dot{h}^* + U_\infty b^2\left(4C(k)c_{0,i} + c_{1,i}\right)\dot{\tau}_i\dot{h}^*$$

$$+\frac{1}{2}U_\infty b^2\left(2c_{0,i} + c_{1,i}\right)\left(C(k)\left(2c_{0,i} - c_{1,i}\right) + c_{1,i}\right)\dot{\tau}_i^2 \tag{3.49}$$

$$+b^3\left(c_{0,i}^2 + \frac{1}{8}c_{1,i}^2 - c_{0,i}c_{2,i} + S_{ii}^6 - S_{ii}^7\right)\dot{\tau}_i\ddot{\tau}_i$$

$$\left.\left.+\frac{1}{2}b^3\left(2c_{0,i} - c_{2,i}\right)\left(\dot{\tau}_i\ddot{h}^* + \ddot{\tau}_i\dot{h}^*\right) + 2U_\infty b^2 C(k)\dot{h}^2 + b^3\dot{h}^*\ddot{h}^*\right]\right\},$$

where the subscript i refers to the ith beam mode and the real part of the complex valued solution is taken. The total power required is the summation of the power due to all the beam modes, given as

$$P'(t^*) = \sum_{i=1}^{\infty} P_i'(t^*). \tag{3.50}$$

CHAPTER 4

RESULTS AND DISCUSSION

Although this model does not enforce any restrictions on the boundary conditions, we turn our attention to the cantilever beam configuration. Significant amount or research has been done using this configuration. It has been used to model paper flutter [34], fuel plates in nuclear reactors [28, 40], chordwise bending of flapping wings in forward flight [37, 38], passive morphing wings [6], to the soft palate that causes snoring in humans [8]. This ample amount of data provides the groundwork for validating the current model. We will define the details of the cantilever beam configuration in Section 4.1. This will be followed by validation of the current models homogeneous and nonhomogeneous solutions to results reported in the literature in Section 4.2. We will then present a study comparing the single-mode and multi-mode solutions in Section 4.3. In this study, we use parameters that represent a typical biological flyer and investigate how flexibility and wing density effect the aerodynamic performance of flapping wings in forward flight.

4.1 Cantilever Beam

The boundary conditions for the cantilever beam are as follows: no displacement or rotation at the leading-edge, $x^*=-1$, and no bending or shear at the trailing-edge, $x^*=1$. The boundary conditions for the beam normal functions for a cantilever beam for $-1 \leq x^* \leq 1$ become

$$\psi\big|_{x^*=-1} = 0, \quad \frac{\partial \psi}{\partial x^*}\bigg|_{x^*=-1} = 0, \quad \frac{\partial^2 \psi}{\partial x^{*2}}\bigg|_{x^*=1} = 0, \quad \frac{\partial^3 \psi}{\partial x^{*3}}\bigg|_{x^*=1} = 0.$$

Evaluating the constants $C_{1,i}$, $C_{2,i}$, $C_{3,i}$ and $C_{4,i}$ in Eq. (2.9) for the above boundary conditions yields the beam normal function for a cantilever beam, given as [52]

$$
\begin{aligned}
\psi_i\left(x^*\right) &= \cosh\left(\frac{\lambda_i}{2}\left(x^*+1\right)\right) - \cos\left(\frac{\lambda_i}{2}\left(x^*+1\right)\right) \\
&\quad - \frac{\cosh\left(\lambda_i\right)+\cos\left(\lambda_i\right)}{\sinh\left(\lambda_i\right)+\sin\left(\lambda_i\right)}\left[\sinh\left(\frac{\lambda_i}{2}\left(x^*+1\right)\right) - \sin\left(\frac{\lambda_i}{2}\left(x^*+1\right)\right)\right],
\end{aligned}
\tag{4.1}
$$

where the eigenvalues, λ_i, are determined by evaluating the transcendental equation,

$$\cos\left(\lambda_i\right)\cosh\left(\lambda_i\right)+1=0. \tag{4.2}$$

The first six consecutive roots of Eq. (4.2) are given in Table 4.1.

Table 4.1. First six consecutive eigenvalues for a cantilever beam.

λ_1	λ_2	λ_3	λ_4	λ_5	λ_6
1.875	4.694	7.855	10.996	14.137	17.279

The Chebyshev coefficients that describe the cantilever beam modes are obtained by evaluating Eq. (3.3) and are shown in Table B.1 in Appendix B for the first six consecutive beam mode shapes. Notice that the higher beam modes have more nonzero coefficients, meaning that a higher number of Chebyshev polynomials are required to describe the shape. This is expected since higher mode shapes contain more curvature. However, the increasing coefficients approach zero asymptotically, and therefore, any truncation error introduced in the aerodynamics model is negligible when sufficiently enough coefficients are considered in the solution.

Figure 4.1 shows the first six conceccutive mode shapes for a cantilever beam comparing the Chebyshev polynomial expansion approxiamation using $n=5$ and $n=20$, where n is the highest number of Chebyshev coefficients considered in the expanssion. The first three consecutive mode shapes are sufficiently recreated using $n=5$, but not sufficient to recrate the fourth or higher modes. The sixth mode shape can be nearly recreated using $n=10$, and with $n=20$ the mode shape is sufficiently recreated. Therefore, in this study, $n=20$ is used to ensure that any truncation error is negligible.

Using the Chebyshev coefficients defined in Appendix B the Chebyshev summations found in Table 3.1 can be evaluated for the cantilever beam configuration. These values are shown in Table C.1 in Appendix C. As mentioned earlier, summations S^1 through S^4 are vectors and S^5 through S^8 are matrices, where S^5, S^6, and S^7 are symmetric and S^8 is skew symmetric.
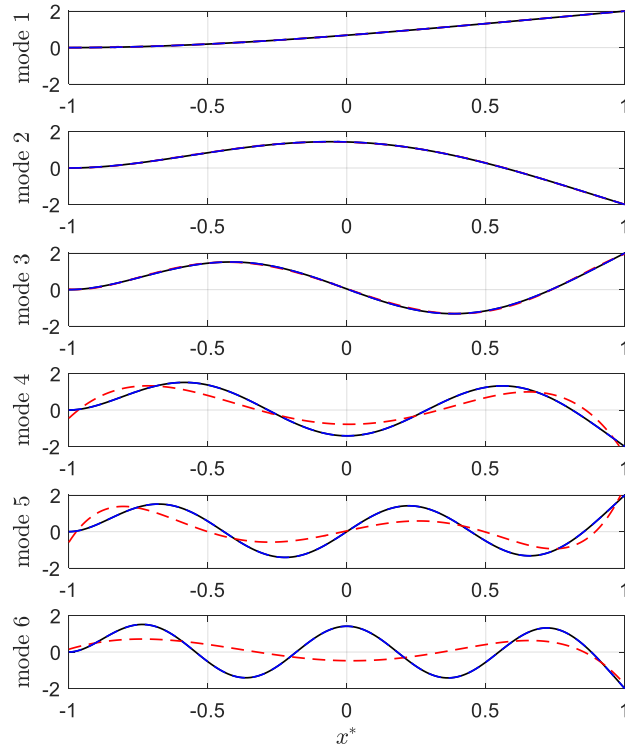
Figure 4.1. First six consecutive mode shapes of the cantilever beam: exact shape (black), Chebyshev recreation using *n*=20 (blue), Chebyshev recreation using *n*=5 (red).

4.2   Model Validation

We first validate the current model by evaluating the homogenous solution and then the inhomogeneous or forced vibration solution. The homogeneous solution provides information about the natural state of the system. In aeroelastic systems, there exists a minimum flow speed and corresponding frequency at which a given structure submerged in a fluid with a given density will exhibit sustained, simple harmonic oscillations [1]. This minimum flow speed is called the flutter speed and it can be obtained for a range of structure configurations defining a neutral stability boundary. This flutter boundary will be used to validate the homogenous solution to the

results found in the literature. The forced vibration model has been used to simulate the chordwise dynamics of that of a flapping wing in forward flight. Such research is done to aid in the understanding of flight performance such as lift, generated thrust, required input power, and propulsion efficiency. Moore [48] has done so using a semi-analytical model, allowing us to validate the current model to these results.

4.2.1   Homogenous Solution Validation

We validate the homogenous solution by comparing the stability boundary to results published by Kornecki et al. [33], Guo & Païdoussis [35], Watanabe et al. [34], and Breuker et al. [6]. Similar to the current model, these four models all utilize the one-dimensional beam equation and two-dimensional incompressible potential flow. Kornecki [33], Guo & Païdoussis [35], and Watanabe et al. [34] use Galerkin's method to solve the structural model, whereas, Breuker et al. [6] uses the Rayleigh Ritz assumed modes method. They also differ in the aerodynamics model, where Kornecki [33] and Breuker et al. [6] used Theodorsen's theory [19] with Glauert's Fourier expansion [16], Watanabe et al. [34] used Küssner's theory [18], and Guo & Païdoussis [35] directly solved the potential equations using Fourier series. It is worth noting that all four models solve the aerodynamics using Fourier series, which makes the current model unique, solving the exact Cartesian integrals for the noncirculatory velocity potential.

Solving Eq. (3.20), the eigenvalues of the homogeneous aeroelastic system can be obtained. The critical or flutter speed of the system occurs when the real part of any eigenvalue becomes positive, indicating negative damping or instability. As previously mentioned, due to the dependence on the frequency, the critical speed must be solved iteratively. To determine the critical flow speed for this study the following procedure was executed. First, the initial flow speed U_0 and frequency guess f_0 are defined. The initial flow speed is chosen such that it is below the critical

flow speed in order to implement a forward marching scheme. The initial frequency guess can be critical for convergence and setting the initial frequency equal to the first bending natural frequency in vacuum often results in the converged solution. With the flow speed and frequency defined, the eigenvalues denoted as s are obtained by performing eigenvalue analysis on the system matrix $\mathbf{A}$, given in Eq. (3.17). If there are no positive real parts in the eigenvalues, indicating negative damping, then the system is stable. The flow speed is increased by a prescribed amount, denoted as ΔU, and eigenvalue analysis is performed on the updated system matrix $\mathbf{A}$. This is repeated until one of the real parts of the eigenvalues becomes positive, indicating positive damping or instability of the system. A frequency error is defined by the difference between the frequency guess and the calculated critical frequency. If the error is greater than the desired frequency tolerance, denoted as ε, then the solution has not converged. A new frequency is defined using a modified bisection method and the flow speed is set equal to the initial flow speed and eigenvalue analysis is performed on the updated system matrix $\mathbf{A}$. This entire routine is repeated until the frequency error is less than the desired tolerance, indicating that the solution has converged and yielding the critical flow speed, U_f, and corresponding frequency, f_f, where the subscript f indicates flutter. A schematic of the process is summarized in Figure 4.2.
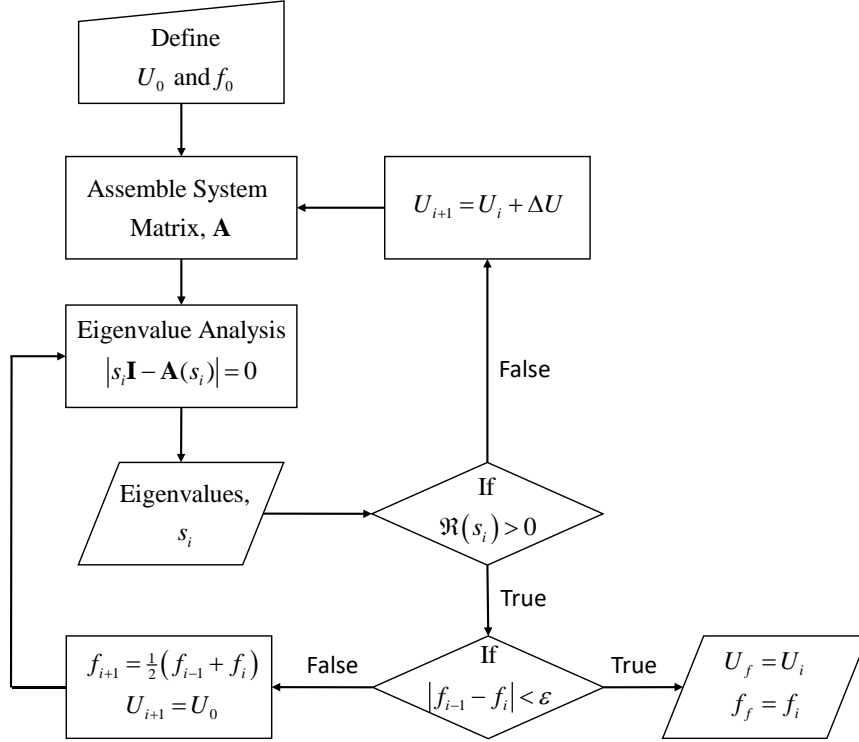
Figure 4.2. Process schematic discribing the iterative scheme used to determine the critical flow speed and frequency.

Let us introduce two independent nondimensional parameters to investigate the trade-space for the stability boundary: mass ratio, M^*, and nondimensional flutter speed, U^*, defined as

$$M^* = \rho^* h_s^*, \quad U^* = \sqrt{\frac{1}{\Pi_1}},$$

where Π_1 is calculated using the flutter speed U_f.

Figure 4.3 shows the relationship of the nondimensional flutter speed and mass ratio comparing the current model to the results published by several researchers. As we move to the

right on the *x*-axis, increasing the mass ratio, the density of the plate is increased and moving up on the *y*-axis indicates a higher flutter speed. We included two sets of results: one using 4 modes (left) and the other using 6 modes (right) in the solution. We have done this for two reasons: first because the results by Watanabe et al. [34] only considered 4 modes in their solution, and second to show how additional modes effect the solution. The stability boundary contains several peaks which correspond to mode switching. When 4 modes are considered in the solution, these peaks are located at M^*=0.152 and 0.690. For M^*<0.152 the 3rd flutter mode is observed, for 0.152<M^*<0.690 the 2nd flutter mode is observed, and for M^*>0.690 the 1st flutter mode is observed. There is good agreement between all of the models at predicting the existence, location and magnitude of these mode switching peaks. When 6 modes are considered in the solution, the peaks move slightly to M^*=0.187 and 0.681 and an additional mode switch is predicted at M^*=0.042, where the 4th flutter mode is observed at mass ratios less than this value. This mode switch is not captured by Watanabe et al. [34], for as you can see in Figure 4.3, 4 modes are not sufficient to predict this aeroelastic response. All models seem to be in good agreement with each other for M^*<1. For M^*>1 discrepancies are apparent in the log-scale. One of the main difference between the current model and the other models is the mathematical model used to solve the unsteady aerodynamics. The current model evaluates the Cartesian integrals exactly in Eq. (2.37) using Chebyshev series, whereas, the other models use Fourier series. As mentioned earlier, Kornecki [33] and Breuker et al. [6] used Theodorsen's [19] theory with Glauert's Fourier expansion [16], Watanabe et al. [34] used Küssner's [18] theory, and Guo & Païdoussis [35] directly solved the potential equations using Fourier series. The aerodynamic theories by Glauert [16] and Küssner [18] are fundamentally similar using a transformation variable and a Fourier expansion. This may be the reason why the results of Kornecki [33], Breuker et al. [6] and

Watanabe et al. [34] show good agreement among each other for $M^*>1$. The solution proposed by Guo & Païdoussis [35] is referred to as a "double wake" solution because it introduces an incoming wake as a result of eliminating both singularities in the pressure difference at the leading and trailing-edges. In order to satisfy the Kutta condition, the trailing-edge singularity must be eliminated, however, the leading-edge singularity should exist, although not physical, this is mathematically correct due to assuming an infinitely thin plate. This additional artificial wake has no significant meaning and has been mentioned that it does not significantly alter the results for the flutter instability [31,33]. However, when Michelin [32] compared his numerical results against a "double wake" model by Eloy [41], there was only good agreement for $M^*<1$, similar to the current situation. After observing this phenomenon, Michelin [32] concluded that for smaller mass ratios, the dominant modes have shorter wave lengths and the dynamics are less influenced by the wake and more by the local displacement of the plate. However, for larger mass ratios, the spatial scale is of order of the length of the plate and is strongly influenced by the description of the wake [32].

Chebyshev series may be more a logical choice for this problem over Fourier series. Although a Chebyshev series is a Fourier cosine expansion with a change variable [55], as mentioned earlier, it is superior at resolving singularities near the endpoints [55]. This is an important characteristic since we know that the perturbation pressure contains a singularity at the leading-edge. Fourier series typically experience Gibbs phenomena at endpoint discontinuities and singularities, which may introduce error in the solution.

Figure 4.4 shows the relationship of the flutter frequency and mass ratio comparing the current model to the results published by Watanabe et al. [34]. In the plot, the frequency is normalized by the 1st natural frequency. Also shown are the values of the 2nd, 3rd, and 4th natural

frequencies, indicated by the dashed lines. As before, we included two sets of results: one using 4 modes (left) and the other using 6 modes (right). The steps in the frequency are observed at the same M^* locations as the peaks in the flutter speed, further indicating mode switching. There is good agreement between the current model considering 4 modes in the solution and the results published by Watanabe et al. [34]. When 6 modes are considered in the solution the additional jump at $M^*=0.045$ is observed, which further indicates an additional mode switch. Additionally, the frequency corresponding to the 3rd flutter mode was affected, which resulted in a lower predicted frequency and the location of the 2nd to 3rd flutter mode transition was slightly shifted, as seen in the flutter speed. Lastly, it was observed that there was little difference between the two models for $M^*>1$, where we observed the greatest discrepancy in the nondimensional flutter speed.
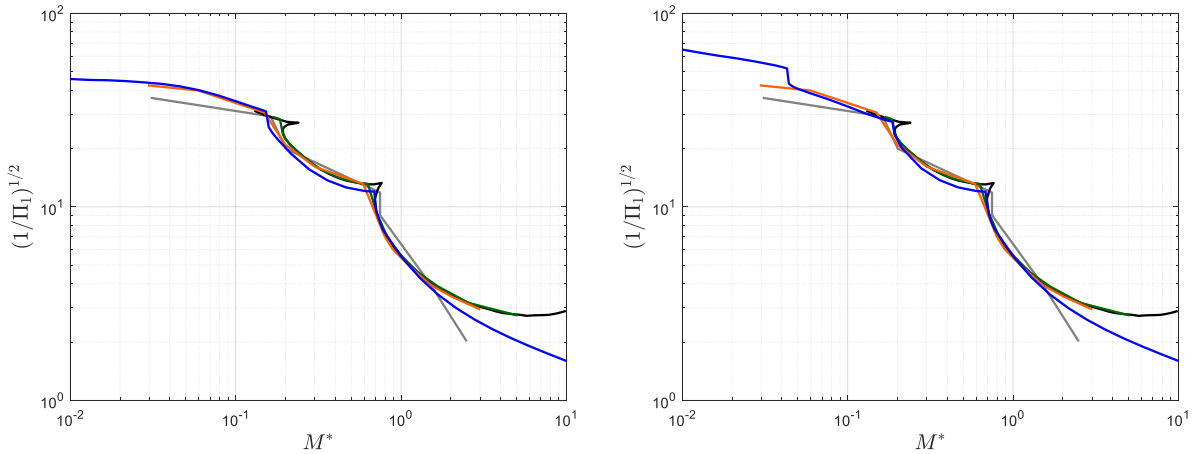

Figure 4.3. Nondimensional flutter speed versus mass ratio. Results include Guo & Païdoussis [35] (grey), Kornecki et al. [33] (black), Breuker et al. [6] (green), Watanabe et al. [34] (orange) and the current model (blue) using 4 modes (left) and using 6 modes (right).
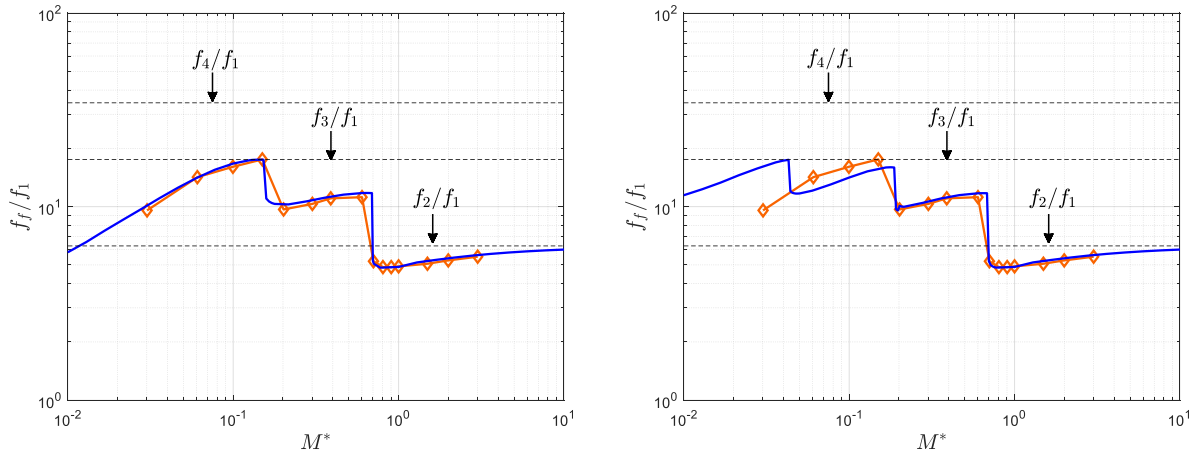
Figure 4.4. Flutter frequency versus mass ratio. Results include Watanabe et al. [34] (orange) and the current model (blue) using 4 modes (left) and using 6 modes (right).

4.2.2 Forced Vibration Solution Validation

We validate the forced vibration response solution by comparing to the results published by Moore [48] for chordwise flexible flapping wings in forward flight. In his study, Moore [48] considers three flexibility arrangements for optimal flexibility for thrust production, one of which is the cantilever beam with uniform stiffness. Identical to the current model, Moore [48] describes the dynamics using the one-dimensional beam equation coupled with two-dimensional potential flow including the trialing-edge vortex shedding. Unlike the current model, Moore [48] solves the two-way nonlocal aeroelastic equation of motion using a semi-analytical method. The equation is discretized using Chebyshev collocation and the linear system is solved iteratively using fast Chebyshev differentiation and a preconditioned Generalized Minimal Residual (GMRES) method. This solution converges on the order $N\text{Log}N$, where N is the number of colocation points, and has been verified to be third-order accurate in space [48]. The aerodynamics in this model are based

on the theory presented by Wu [10], which utilizes Küssner's theory [18]. Moore [48] introduces a normalized thrust and power coefficient defined as,

$$\tilde{c}_T = \frac{\langle T' \rangle}{\frac{1}{2}\pi^3 \rho_f f^2 (2h_a)^2 c}, \quad \tilde{c}_P = \frac{\langle P' \rangle}{\frac{1}{2}\pi^3 \rho_f f^2 (2h_a)^2 Uc}, \tag{4.3}$$

where T' and P' are the instantaneous thrust and input power per unit span, respectively, and the brackets $\langle\ \rangle$ indicate a time average over one flapping cycle. The convenience of defining the thrust and power coefficients in this form is that they become independent of the driving amplitude, and thus eliminating one parameter from the trade-space [48]. Using the mass ratio M^*, which is equivalent to the density parameter R as used by Moore [48], and effective inertia Π_1, which is equal to 1/12 times the flexibility wing parameter S as used by Moore [48], all possible material distributions are explored within a chosen range of reduced frequencies.

Figure 4.5 shows the thrust and power coefficient as well as the propulsion efficiency versus reduced frequency comparing the current model to the results published by Moore [48]. The results are obtained by varying the reduced frequency, while fixing M^*=1 and considering various values of Π_1. For these results, we used 6 modes in the solution. There is good agreement between the two models, with the only discrepancy being the amplitude of the peaks. The current model consistently predicts a slightly larger peak value for the thrust and input power coefficients for all the considered values of Π_1. The thrust coefficient peaks are observed at k=1.80, 1.55 and 1.24 for Π_1=5/3, 5/4 and 5/6, respectively. The power coefficient peaks are observed at k=1.81, 1.57 and 1.27 for Π_1=5/3, 5/4 and 5/6, respectively. The largest difference of 16 percent is observed for C_T at Π_1=5/6. It is worth noting that Moore's [48] model is semi-analytical, and therefore, still

requires to be solved numerically, whereas the current model gives the exact solution in closed-form.

The propulsion efficiency is defined as the ratio of the thrust and the input power given as $\tilde{c}_T/\tilde{c}_p$. The results indicate that there is a reduced frequency value, of which, when below this value a slight increase in propulsion efficiency is gained for the flexible wing as compared to the rigid wing. These values are observed at k=1.04, 0.93 and 0.80 for Π_1=5/3, 5/4 and 5/6, respectively. However, once past this value the propulsion efficiency for the flexible wing remains lower than that of the rigid wing. This trend is observed for all considered values of Π_1. It was observed that Moore's [48] published results for the propulsion efficiency do not agree with the published results for the thrust and power coefficient. This is why large discrepancies are observed between the current model and Moore's [48] results for the propulsion efficiency, but not for the thrust and power coefficients.
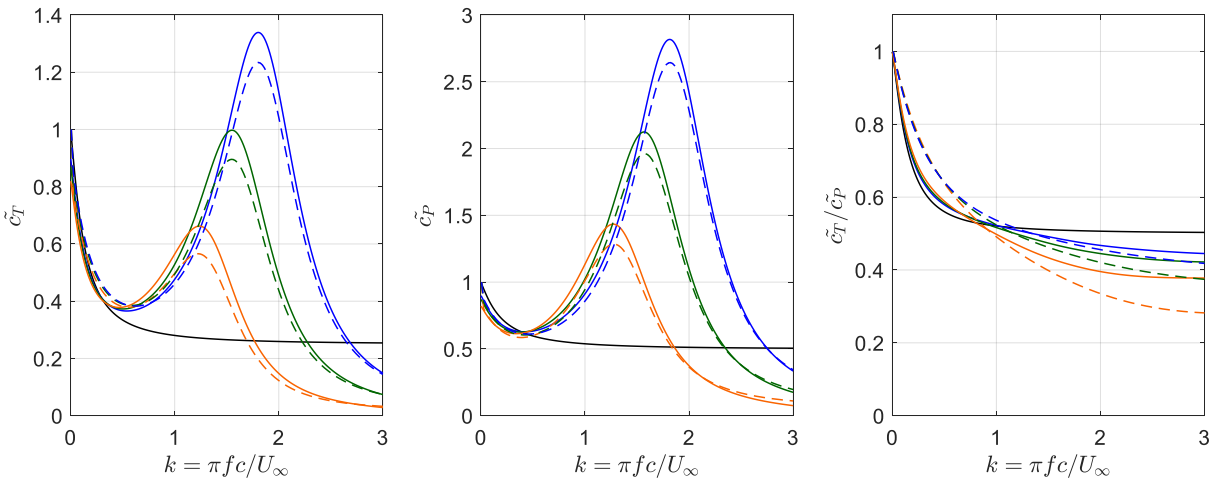

Figure 4.5. Mean thrust coefficient (left), mean power coefficient (middle) versus reduced frequency, and propulsion efficiency (right), for Π_1=∞ (black), Π_1=5/3 (blue), Π_1=5/4 (green) and Π_1=5/6 (orange). Results include Moore [48] (dashed) and the current model (solid).

4.3 Comparison of the Single-mode and Multi-mode Solutions

In this section we compare and discuss the local single-mode solution, presented in Section 3.3.3, to the nonlocal multi-mode solution, presented in Section 3.3.2. The single-mode solution neglects any higher mode contribution, and therefore, is only valid when the first mode dominates the aeroelastic response. In Section 3.3.3 we introduced the frequency ratio, f_1^*, defined as

$$f_1^* = \frac{f}{f_1} = \sqrt{\frac{\Pi_0}{\Pi_1} \frac{4\pi^2}{\lambda_1^4}}, \tag{3.31}$$

which can be used as a crude indication for when the single-mode solution yields equivalent or sufficiently accurate results in comparison to the exact multi-mode solution.

We introduce the normalized trailing-edge amplitude, $w_{TE}^* = w^*(1, t^*)$, and the lift coefficient, c_L, thrust coefficient, c_T, and power coefficient, c_P, defined as

$$c_L = \frac{L'}{\frac{1}{2}\rho_f U_\infty^2 c}, \quad c_T = \frac{\langle T'\rangle}{\frac{1}{2}\rho_f U_\infty^2 c}, \quad c_P = \frac{\langle P'\rangle}{\frac{1}{2}\rho_f U_\infty^3 c}, \tag{4.4}$$

respectively, where the brackets $\langle\,\rangle$ indicate a time average over one flapping cycle. We consider the maximum lift to calculate the lift coefficient. We calculate an error between the single-mode and multi-mode solutions defined as the absolute value of the difference between the multi-mode and single-mode solutions divided by the multi-mode solution, given as

$$error(\cdot) = abs\left[\frac{(\cdot)_{\text{Multi}} - (\cdot)_{\text{Single}}}{(\cdot)_{\text{Multi}}}\right]. \tag{4.5}$$

For this study we use parameters that represent a typical biological flyer. We set the reduced frequency to $k=0.3$ and the Strouhal number to $St=0.3$ [2]. Since the analysis is no longer sensitive to the chord or flapping frequency, these parameters were set equal to unity. Furthermore, the fluid density is set equal to 1.2 kg/m^3 representing air. We change the value of Young's modulus, which changes the value of the effective stiffness, Π_1, to obtain the various values of $f_1{}^*$. To study the effect that the wing mass has on the solution, we consider three different values of effective mass, $\Pi_0=0.01$, 0.02 and 0.03.

The maximum normalized trailing-edge amplitude as a function of frequency ratio is shown in Figure 4.6. The corresponding error between the single-mode and multi-mode solutions for the maximum trailing-edge amplitude are shown in Figure 4.7. At $f_1{}^*=0$ the trailing-edge amplitude is zero, which represents the rigid wing case. Visually the single-mode solution yields similar results to that of the multi-mode solution up to $f_1{}^*=0.6$ for all values of Π_0 considered. Beyond $f_1{}^*=0.6$ the single-mode overpredicts the trailing-edge amplitude, however, the general trend is still captured up to $f_1{}^*=1$. The single-mode solution produces an error of 5% starting at $f_1{}^*=0.76$ and an error of 10% is observed starting at $f_1{}^*=0.91$ for the values of Π_0 considered. In general, the trailing-edge amplitude increases with increasing $f_1{}^*$, however, a maximum is reached. There is a threshold value of $f_1{}^*$, for when below this value smaller values of Π_0 yield larger trailing-edge amplitudes, however, above this value larger values of Π_0 produce larger trailing-edge amplitudes. This threshold is located near $f_1{}^*=0.4$ for the values of Π_0 considered. For $\Pi_0=0.01$ the trailing-edge amplitude reaches a maximum of $w_{TE}{}^*=1.25$ at $f_1{}^*=0.92$ for the multi-mode solution. For $\Pi_0=0.02$ and $\Pi_0=0.03$ the trailing-edge amplitudes reach maximums at $f_1{}^*>1$. Additionally, when $w_{TE}{}^*>2$, as seen for $\Pi_0=0.03$, the wing deformations are large, implying that the employed linear beam model may introduce errors into the solution.

Figure 4.6. Maximum normalized trailing-edge amplitude versus frequency ratio for Π_0=0.01 (blue), Π_0=0.02 (green) and Π_0=0.03 (orange): mulit-mode solution using 6 modes (solid) and single-mode solution (dashed).

Figure 4.7. Error of the maximum normalized trailing-edge amplitude between the single-mode and multi-mode solution versus frequency ratio for Π_0=0.01 (blue), Π_0=0.02 (green) and Π_0=0.03 (orange).

Figure 4.8 shows the lift coefficient as a function of the frequency ratio. The corresponding errors between the single-mode and multi-mode solutions for the lift coefficient are shown in Figure 4.9. Visually the single-mode solution yields similar results to that of the multi-mode solution up to $f_1{}^*$=0.6 for Π_0=0.01, $f_1{}^*$=0.7 for Π_0=0.02 and $f_1{}^*$=0.8 for Π_0=0.03. Beyond these values the single-mode overpredicts the maximum lift, however, the general trend is still captured up to $f_1{}^*$=1. The single-mode solution produces an error of 5% starting at $f_1{}^*$=0.6 and a 10% error is observed starting at $f_1{}^*$=0.75 for the values of Π_0 considered. At $f_1{}^*$=0 the maximum lift is c_L=3.15, which represents the rigid wing case. As $f_1{}^*$ increases, the maximum lift decreases reaching minimums of c_L=2.74 at $f_1{}^*$=0.59 for Π_0=0.02 and c_L=3.12 at $f_1{}^*$=0.21 for Π_0=0.03 for the multi-mode solution. A minimum is not observed for Π_0=0.01 within the range of $f_1{}^*$ considered. For Π_0=0.02, the maximum lift increases slightly reaching a peak at c_L=2.78 at $f_1{}^*$=0.91 and slightly decreasing thereafter as $f_1{}^*$ increases for the multi-mode solution. For Π_0=0.03, the maximum lift increases as $f_1{}^*$ increases, passing through a point at which the wing produces more maximum lift than its rigid wing counterpart. This location is observed at $f_1{}^*$=0.31 for the multi-mode solution. This indicates that for the chosen parameters, a denser wing will produce more maximum lift then its lesser dense wing counterpart. In summary, there is threshold value of Π_0 for which below this value a flexible wing will never produce more maximum lift than its rigid wing counterpart. However, when above this value, a flexible wing can produce more maximum lift than its rigid wing counterpart.
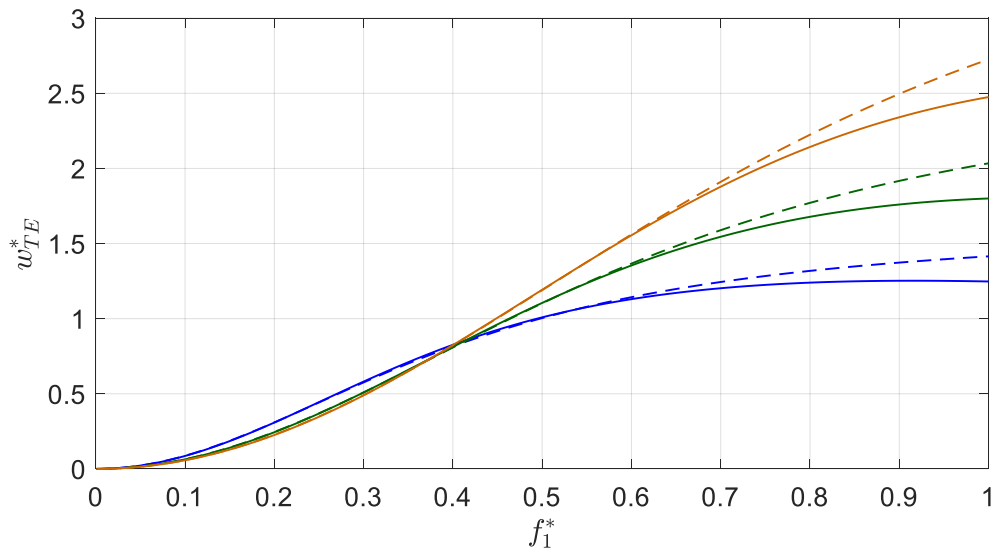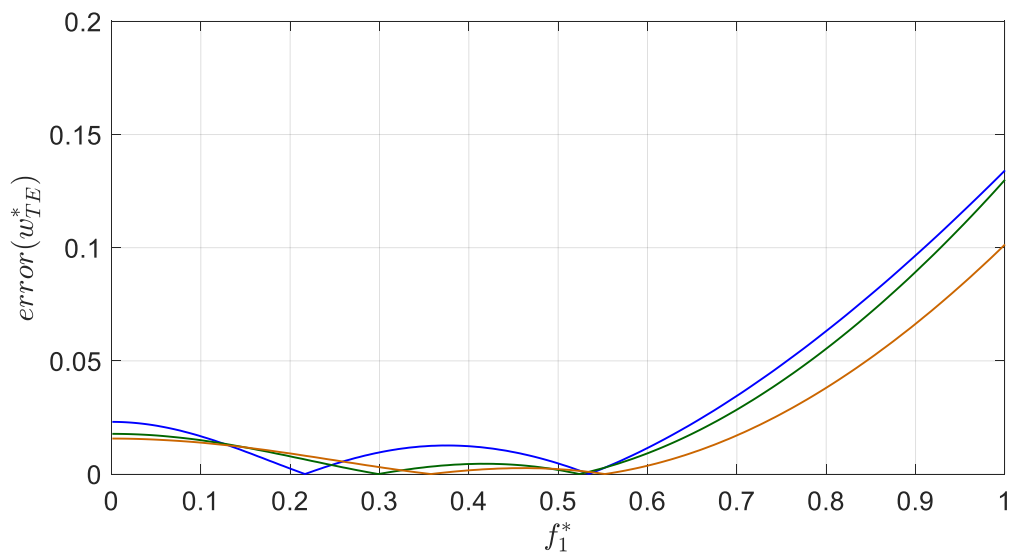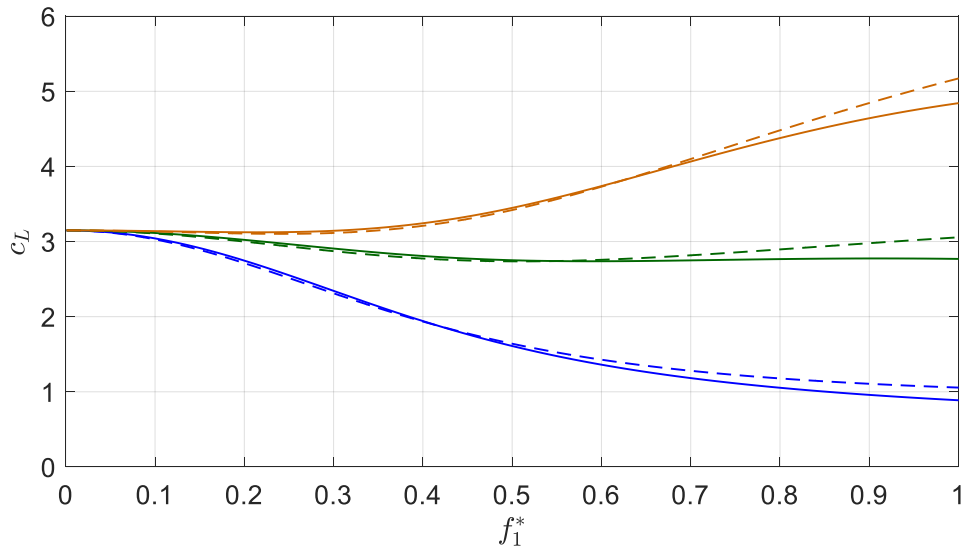
Figure 4.8. Maximum lift coefficient versus frequency ratio for $\Pi_0=0.01$ (blue), $\Pi_0=0.02$ (green) and $\Pi_0=0.03$ (orange): mulit-mode solution using 6 modes (solid) and single-mode solution (dashed).
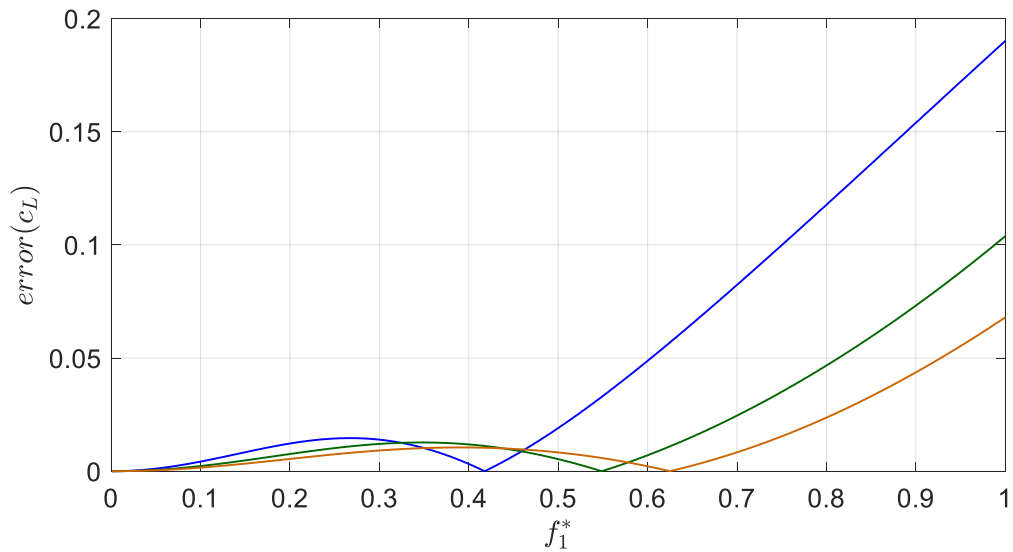

Figure 4.9. Error of the maximum lift coefficient versus frequency ratio for $\Pi_0=0.01$ (blue), $\Pi_0=0.02$ (green) and $\Pi_0=0.03$ (orange).

The mean thrust coefficient as a function of frequency ratio is shown in Figure 4.10. The corresponding errors between the single-mode and multi-mode solutions for the mean thrust are shown in Figure 4.11. Visually the single-mode solution yields similar results to that of the multi-mode solution up to $f_1^*=0.7$ for all values of Π_0 considered. Beyond this point, the single-mode underpredicts the mean thrust, however, the general trend is still captured up to $f_1^*=1$. The single-mode solution produces an error of 5% starting at $f_1^*=0.69$ and an error of 10% starting at $f_1^*=0.71$ for the values of Π_0 considered. At $f_1^*=0$ the thrust coefficient is $c_T=1.14$, which represents the rigid wing case. As f_1^* increases, the mean thrust slightly increases to $c_T=1.15$ at $f_1^*=0.12$ for $\Pi_0=0.01$, $c_T=1.18$ at $f_1^*=0.22$ for $\Pi_0=0.02$ and $c_T=1.20$ at $f_1^*=0.27$ for $\Pi_0=0.03$ for the multi-mode solution. From this, it appears that denser wings have the potential to yield a larger maximum mean thrust at certain f_1^*. As f_1^* further increases, the mean thrust decreases passing through a point for which the wing produces less mean thrust than its rigid wing counterpart. These locations are observed at $f_1^*=0.17$ for $\Pi_0=0.01$, $f_1^*=0.32$ for $\Pi_0=0.02$ and $f_1^*=0.39$ for $\Pi_0=0.03$ for the multi-mode solution. For $\Pi_0=0.01$, a minimum is observed at $f_1^*=1$ for the multi-mode solution and for $\Pi_0=0.02$ and $\Pi_0=0.03$ minimums are reached at $f_1^*>1$. It appears that denser wings can yield lower minimum mean thrust at certain f_1^*. Additionally, for $\Pi_0=0.03$, negative thrust is observed at $f_1^*=0.80$ for the multi-mode solution. In summary, there is a threshold value of f_1^*, for when below this value a denser wing can produce more mean thrust than its rigid wing counterpart, and increasing density increases the generated mean thrust. Beyond this threshold value of f_1^*, flexible wings will produce less mean thrust than its rigid wing counterpart. However, there is a threshold value of Π_0 for which a flexible wing will never produce more mean thrust than its rigid wing counterpart. Additionally, there is another threshold value of f_1^* beyond the first threshold value, for which a lesser dense wing will produce more mean thrust than its denser wing counterpart.
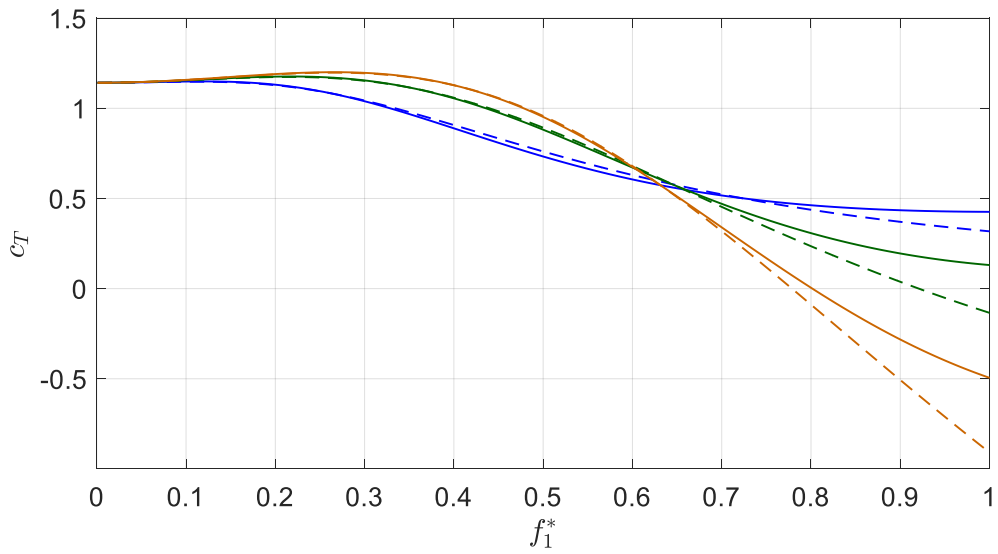
Figure 4.10. Mean thrust coefficient versus frequency ratio for Π_0=0.01 (blue), Π_0=0.02 (green) and Π_0=0.03 (orange): mulit-mode solution using 6 modes (solid) and single-mode solution (dashed).

Figure 4.11. Error of the mean thrust coefficient versus frequency ratio for Π_0=0.01 (blue), Π_0=0.02 (green) and Π_0=0.03 (orange).

The mean power coefficient as a function of frequency ratio is shown in Figure 4.12. The corresponding errors between the single-mode and multi-mode solutions for the mean power are shown in Figure 4.13. Visually the single-mode solution yields similar results to that of the multi-mode solution up to $f_1{}^*$=0.5 for Π_0=0.01, $f_1{}^*$=0.6 for Π_0=0.02 and $f_1{}^*$=0.7 for Π_0=0.03. Beyond these locations the single-mode slightly overpredicts the mean power, however, the general trend is still captured up to $f_1{}^*$=1. The single-mode solution produces an error of 5% starting at $f_1{}^*$=0.66 and an error 10% was never reached for the values of Π_0 considered. A maximum error of 6.8% is observed at $f_1{}^*$=0.93 for Π_0=0.03. From Figure 4.12, it appears that denser wings require more power to flap. This makes physical sense, for it takes more energy to move a heavier object. At $f_1{}^*$=0 the power coefficient is c_P=1.85, which represents the rigid wing case. For Π_0=0.01 the mean power continuously decreases as $f_1{}^*$ increases. However, for Π_0=0.02 and Π_0=0.03 the mean power slightly increases reaching maximums of c_P=1.86 at $f_1{}^*$=0.15 for Π_0=0.02 and c_P=1.93 at $f_1{}^*$=0.32 for Π_0=0.03 for the multi-mode solution. Thereafter, the mean power decreases as $f_1{}^*$ increases passing through a point for which the plate requires less power than the rigid wing counterpart. These locations are observed at $f_1{}^*$=0.21 for Π_0=0.02 and $f_1{}^*$=0.48 for Π_0=0.03 for the multi-mode solution. The mean power approaches minimums at $f_1{}^*$>1. In summary, there is a threshold value of $f_1{}^*$, for when below this value, denser wings may require more power to flap than its rigid wing counterpart, however, above this value less power is required than its rigid wing counterpart. Furthermore, there is a threshold value of Π_0 for which lesser dense wings will never require more power than its rigid wing counterpart.

Figure 4.12. Mean power coefficient versus frequency ratio for Π_0=0.01 (blue), Π_0=0.02 (green) and Π_0=0.03 (orange): mulit-mode solution using 6 modes (solid) and single-mode solution (dashed).
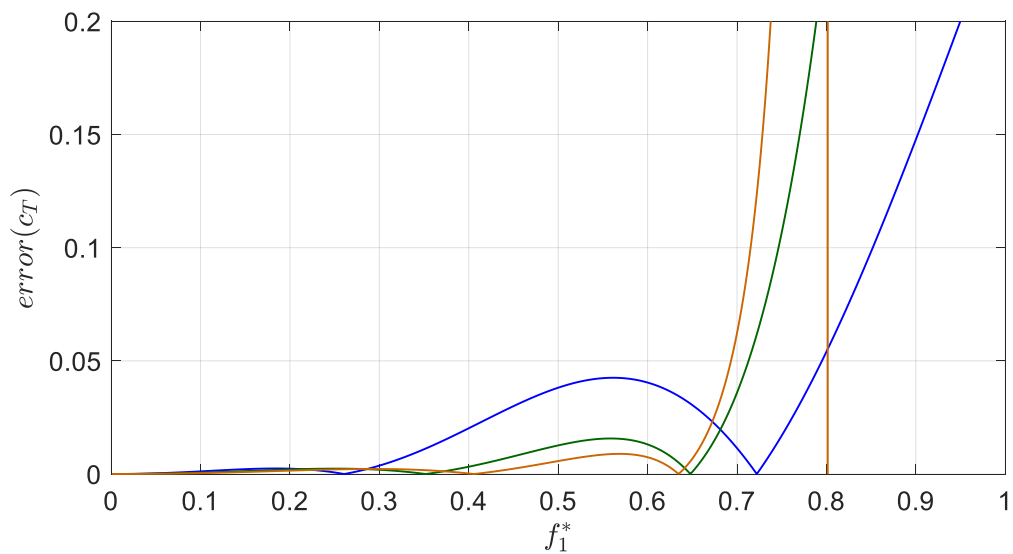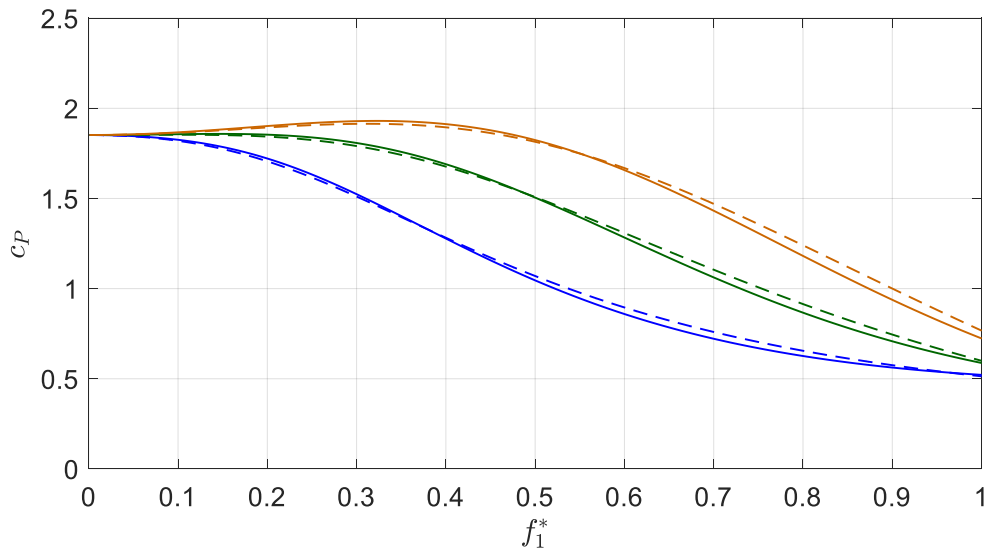

Figure 4.13. Error of the mean power coefficient versus frequency ratio for Π_0=0.01 (blue), Π_0=0.02 (green) and Π_0=0.03 (orange).

The propulsion efficiency as a function of reduced frequency is shown in Figure 4.14. The corresponding errors between the single-mode and multi-mode solutions for the propulsion efficiency are shown in Figure 4.15. Visually the single-mode solution yields similar results to that of the multi-mode solution up to $f_1^*=0.6$ for all values of Π_0 considered. When $f_1^*>0.6$ the single-mode solution underpredicts the propulsion efficiency and unlike the other results, the single-mode does not appear to capture the general trend of the multi-mode solution as f_1^* approaches 1. The single-mode solution produces an error of 5% starting at $f_1^*=0.68$ and a 10% error is observed as early as $f_1^*=0.71$ for the values of Π_0 considered. The propulsion efficiency initially starts at $c_T/c_P=0.62$, which is equivalent to the rigid wing case. For $\Pi_0=0.01$ the efficiency continuously increases with increasing f_1^* where it appears to plateau between $0.4<f_1^*<0.6$ and more rapidly increases as f_1^* increases for the multi-mode solution. For $\Pi_0=0.02$ and $\Pi_0=0.03$ the efficiency slightly increases reaching maximums of $c_T/c_P=0.64$ at $f_1^*=0.28$ for $\Pi_0=0.02$ and $c_T/c_P=0.63$ at $f_1^*=0.22$ for $\Pi_0=0.03$ for the multi-mode solution. As f_1^* further increases the propulsion efficiency decreases passing through a point for which the propulsion efficiency becomes less than that of the rigid wing counterpart. These locations are observed at $f_1^*=0.43$ for $\Pi_0=0.02$ and $f_1^*=0.32$ for $\Pi_0=0.03$ for the multi-mode solution. A minimum is observed for $\Pi_0=0.02$ slightly beyond $f_1^*=1$. Negative values are obtained for $\Pi_0=0.03$ at $f_1^*=0.80$ due to the production of negative thrust. In summary, up to a certain threshold value of f_1^*, flexible wings experience an increase in propulsion efficiency over its rigid wing counterpart. Beyond this threshold value of f_1^*, for denser wings, the propulsion efficiency continuously decreases as f_1^* approaches 1. However, there is threshold value of Π_0 for which a flexible wing will always be more efficient than its rigid wing counterpart.
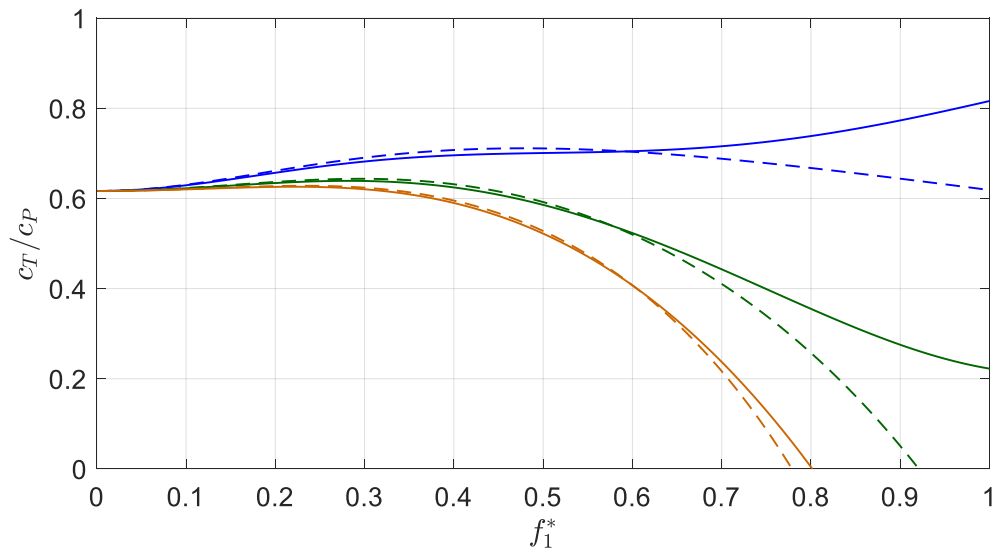
Figure 4.14. Propulsion efficiency versus frequency ratio for $\Pi_0=0.01$ (blue), $\Pi_0=0.02$ (green) and $\Pi_0=0.03$ (orange): mulit-mode solution using 6 modes (solid) and single-mode solution (dashed).
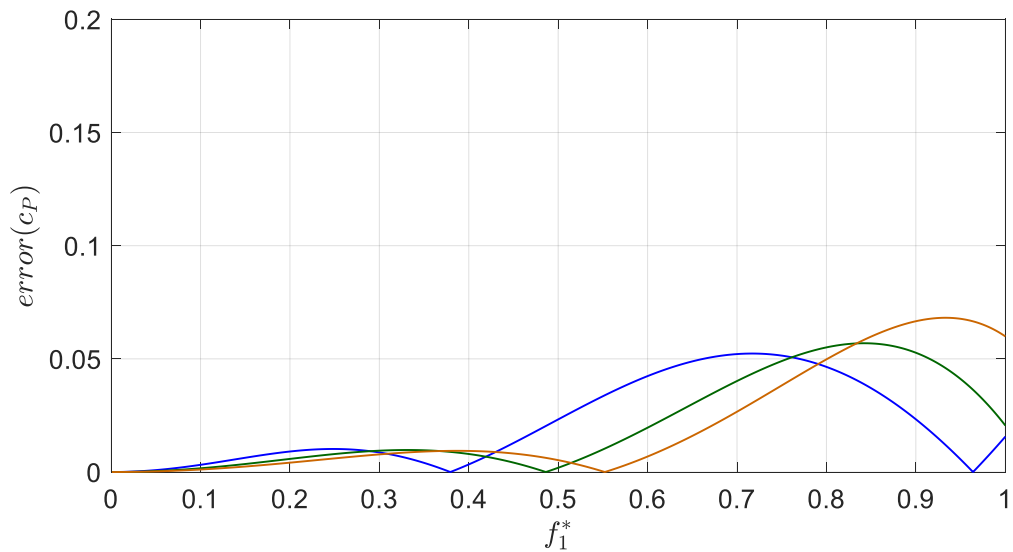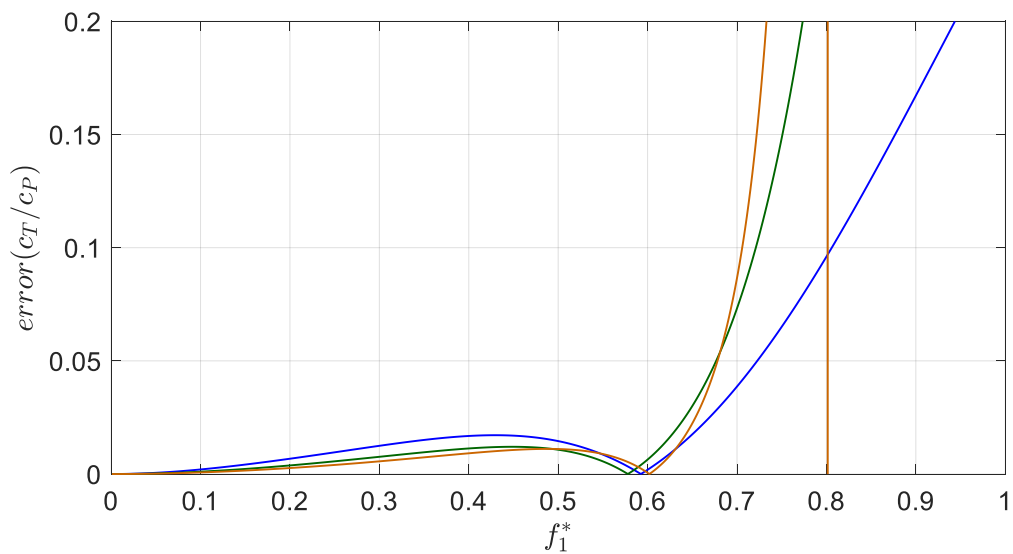

Figure 4.15. Error of the propulsion efficiency versus frequency ratio for $\Pi_0=0.01$ (blue), $\Pi_0=0.02$ (green) and $\Pi_0=0.03$ (orange).

CHAPTER 5

CONCLUSION

5.1   Conclusion

A closed-form analytical solution has been presented for the two-way coupled, two-dimensional unsteady aeroelastic dynamic response of an elastic plate immersed in an axial potential flow. We have chosen to focus our attention on an analytical solution, because of the benefits an analytical solution can provide for understanding the mechanism of FSI. Although analytical models have been developed and previously presented, to our knowledge, a closed-form analytical solution to this two-way coupled aeroelastic problem has not been presented in the literature. Furthermore, all integrations and solutions are exact.

The presented analytical model can predict the two-way coupled aeroelastic dynamic response of a two-dimensional elastic plate immersed in an axial flow. The solution accounts for an imposed plunging motion and the effects of plate curvature along the flow direction. The model couples linearized beam theory and thin airfoil theory for deformable airfoils to develop an equation of motion that dynamically balances the inertia, elastic and aerodynamic forces.

Implementing Galerkin's method, the plate deformation is expressed as the linear summation of the products of the beam normal functions and unknown temporal solutions. Utilizing the orthogonality relationship of the normal functions, the equations of motion reduce to N number of nonlocal second order ordinary differential equations with the temporal solution as the unknown variable. By expressing the beam normal functions in a Chebyshev polynomial expansion, the unsteady aerodynamic pressure is derived with respect to the beam normal functions as a function of the unknown temporal solution. From this, the generalized aerodynamic load can be expressed in closed-form with the temporal solution as the unknown variable. The nonlocal equations of motion can be solved using existing analytical methods. Furthermore, closed-form solutions are obtained for the lift force, generated thrust, required input power and propulsion efficiency.

The current model's homogeneous and inhomogeneous solutions were validated against results found in the literature. Stability analysis was performed for a range of mass ratios obtaining the flutter speeds and corresponding frequencies. There is good agreement between all of the analytical models, where similar trends are observed identifying and locating mode switches. It was observed that the largest discrepancies for the flutter speed appeared for $M^*>1$. Kornecki [33], Watanabe et al. [34], and Breuker et al. [6] show good agreement against one another in this region, however, this could be due to the similarities in the solution of the aerodynamic model, where Fourier series is utilized. Guo & Païdoussis [35] solution showed discrepancies for mass ratio less than 0.01 and greater than 1. This could be due to the effect of the "double wake" that is inherited in the aerodynamic solution by eliminating both singularities in the perturbation pressure at the leading and trailing-edges. Chebyshev series are used in the current model, which may be more appropriate for this problem, due to its capability of resolving endpoint singularities.

The inhomogeneous or forced solution is compared to the results published by Moore [48] comparing thrust and power input for a range of reduced frequencies. The two models produce similar results, with the current model consistently predicting a slightly larger maximum value. The model presented by Moore [48] is a semi-analytical model and requires to be solved numerically, whereas the current model is a closed-form analytical solution.

A comparison of the single-mode solution to the multi-mode solution was presented by studying the chordwise flexibility of an average biological flyer wing investigating the aerodynamic performance as a function of frequency ratio. We considered three different values of effective mass. Results for the normalized trailing-edge amplitude, maximum lift coefficient, mean thrust coefficient, mean power coefficient, and propulsion efficiency were plotted against frequency ratio for both the single-mode and multi-mode solutions. For the selected parameters, the single-mode solution produced similar results to that of the multi-mode solution up to certain values of f_1^*. Additionally, the errors between the single-mode and multi-mode solutions were plotted against frequency ratio for each result. Errors of 5% were observed starting at $f_1^*=0.6$ and errors of 10% were observed starting at $f_1^*=0.71$ for the values of Π_0 considered. However, this may not be the case for all configurations, and will depend on the amount of aerodynamic influence on the solution. Furthermore, in this study we observed the following:

1) There is a threshold value of Π_0, for when below this value lesser dense wings yield larger trailing-edge amplitudes and when above this value denser wings yield larger trailing edge displacements.

2) There is threshold value of Π_0 for which below this value, a flexible wing will never produce more maximum lift than its rigid wing counterpart. However, when above this value, a flexible wing can produce more maximum lift than its rigid wing counterpart.

82

3) There is a threshold value of $f_1{}^*$, for when below this value a denser wing can produce more mean thrust than its rigid wing counterpart, and increasing density increases the generated mean thrust. Beyond this threshold value of $f_1{}^*$, flexible wings will produce less mean thrust than its rigid wing counterpart. However, there is a threshold value of Π_0 for which a flexible wing will never produce more mean thrust than its rigid wing counterpart. Additionally, there is another threshold value of $f_1{}^*$ beyond the first threshold value, for which a lesser dense wing will produce more mean thrust than a denser wing.

4) Beyond a certain flexible and density threshold negative thrust can be observed, resulting in aerodynamic drag. This is consistent with the findings of Heathcote et al. [44] and Michelin et al. [50], who observed similar trends in their experiments. They concluded that a little flexibly can lead to an increase in thrust, however, too much flexibility leads to drag.

5) There is a threshold value of $f_1{}^*$, for when below this value denser wings may require more power to flap than its rigid wing counterpart, however, above this value less power is required than its rigid wing counterpart. Furthermore, there is a threshold value of Π_0 for which lesser dense wings will never require more power than its rigid wing counterpart.

6) Up to a certain threshold value of $f_1{}^*$, flexible wings experience an increase in propulsion efficiency over its rigid wing counterpart. Beyond this threshold value of $f_1{}^*$, for denser wings, the propulsion efficiency continuously decreases as $f_1{}^*$ approaches 1. However, there is a threshold value of Π_0 for which a flexible wing will always be more efficient than its rigid wing counterpart.

5.2   Novel Contributions

This work has focused on advancing the analytical tools for aeroelastic problems. The research has provided the following novel contributions:

1) Expressing the generalized aerodynamic force, lift, thrust, and power in closed-form as a function of the unknown temporal solution.

2) Presenting a closed-form solution to the two-way coupled, two-dimensional unsteady aeroelastic dynamic response of an elastic plate immersed in an axial potential flow.

3) Unlike other analytical models which used Fourier series, the current solution was obtained using Chebyshev series, which are superior at resolving endpoint singularities.

5.3   Future Work

Future work of this two-dimensional model and methodology include the following:

1) Study flight performance of flapping wings in forward flight for either insects or birds. By using this closed-form analytical solution, we hope to help close the gap of our understanding of this FSI problem.

2) Aid in the understanding of hydrodynamic damping in dense fluids. We hope to utilize the closed-form analytical solution to derive correlations between parameters to predict the hydrodynamic damping in turbomachinery inducer blades.

3) Expand the capability of this two-dimensional model to account for three-dimensional effects by coupling the spanwise and chordwise flexibility mechanisms.

4) Further investigate using Chebyshev versus Fourier series in the solution of the aerodynamics.

APPENDIX A

Integral Solutions

Table A.1. Solutions to the integral found in the noncirculatory velocity potential.

n	$\displaystyle\int_{-1}^{1} x_1^{*n} \log\left[\frac{(x^*-x_1^*)^2 + \left(\sqrt{1-x^{*2}} - \sqrt{1-x_1^{*2}}\right)^2}{(x^*-x_1^*)^2 + \left(\sqrt{1-x^{*2}} + \sqrt{1-x_1^{*2}}\right)^2} \right] dx_1^*$
0	$-2\pi\sqrt{1-x^{*2}}$
1	$-\pi x^*\sqrt{1-x^{*2}}$
2	$\dfrac{\pi(x^*-1)(x^*+1)(2x^{*2}+1)}{3\sqrt{1-x^{*2}}}$
3	$\dfrac{\pi x^*(x^*-1)(x^*+1)(2x^{*2}+1)}{4\sqrt{1-x^{*2}}}$
4	$\dfrac{\pi(x^*-1)(x^*+1)(8x^{*4}+4x^{*2}+3)}{20\sqrt{1-x^{*2}}}$
5	$\dfrac{\pi x^*(x^*-1)(x^*+1)(8x^{*4}+4x^{*2}+3)}{24\sqrt{1-x^{*2}}}$
6	$\dfrac{\pi(x^*-1)(x^*+1)(16x^{*6}+8x^{*4}+6x^{*2}+5)}{56\sqrt{1-x^{*2}}}$

APPENDIX B

Chebyshev Coefficients

Table B.1. Chebyshev coefficients for cantilever beam first six consecutive mode shapes.

c_n	Mode 1	Mode 2	Mode 3	Mode 4	Mode 5	Mode 6
c_0	0.836668	0.043313	0.418008	0.010756	0.305914	0.005516
c_1	1.039859	-0.845595	0.107454	-0.630920	0.044792	-0.518382
c_2	0.160456	-1.205177	0.469596	-0.329938	0.451475	-0.166987
c_3	-0.040308	-0.145145	1.206252	-0.290000	0.517302	-0.318671
c_4	0.002855	0.170134	0.101022	-1.122306	0.187280	-0.647345
c_5	0.000451	-0.008977	-0.349976	-0.068698	0.965360	-0.124188
c_6	0.000021	-0.008485	0.010690	0.527571	0.046821	-0.754097
c_7	-0.000002	-0.000278	0.038470	-0.009486	-0.681050	-0.032130
c_8	0.000000	0.000218	0.000657	-0.094960	0.007581	0.793803
c_9	0.000000	-0.000005	-0.002284	-0.000841	0.176987	-0.005782
c_{10}	0.000000	-0.000003	0.000026	0.009458	0.000847	-0.278994
c_{11}	0.000000	0.000000	0.000086	-0.000051	-0.025672	-0.000757
c_{12}	0.000000	0.000000	0.000001	-0.000607	0.000068	0.054496
c_{13}	0.000000	0.000000	-0.000002	-0.000002	0.002428	-0.000074
c_{14}	0.000000	0.000000	0.000000	0.000027	0.000004	-0.006980
c_{15}	0.000000	0.000000	0.000000	0.000000	-0.000163	-0.000006
c_{16}	0.000000	0.000000	0.000000	-0.000001	0.000000	0.000639
c_{17}	0.000000	0.000000	0.000000	0.000000	0.000008	0.000000
c_{18}	0.000000	0.000000	0.000000	0.000000	0.000000	-0.000044
c_{19}	0.000000	0.000000	0.000000	0.000000	0.000000	0.000000
c_{20}	0.000000	0.000000	0.000000	0.000000	0.000000	0.000002

APPENDIX C

Chebyshev Summations

Table C.1. Chebyshev summation values for a cantilever beam.

n	S^n
1	$\begin{bmatrix} 1.2536 & -3.1069 & 3.6389 & -4.5747 & 4.9989 & -5.7034 \end{bmatrix}$
2	$\begin{bmatrix} 0.3325 & -1.7790 & 1.4129 & -2.6557 & 2.0030 & -3.3217 \end{bmatrix}$
3	$\begin{bmatrix} 0.9212 & -1.3279 & 2.2260 & -1.9190 & 2.9959 & -2.3817 \end{bmatrix}$
4	$\begin{bmatrix} 0.1662 & -0.8895 & 0.7065 & -1.3278 & 1.0015 & -1.6609 \end{bmatrix}$
5	$\begin{bmatrix} 1.1377 & -1.2466 & 0.1169 & -0.7398 & 0.1332 & -0.5619 \\ & 3.7998 & -1.6642 & 0.6674 & -1.2683 & 0.5845 \\ & & 5.4821 & -1.7296 & 0.5032 & -1.4628 \\ & & & 7.6736 & -1.7621 & 0.6485 \\ & & & & 9.5620 & -1.7748 \\ & & & & & 11.6577 \end{bmatrix}_{sym}$

6	$\begin{bmatrix} 0.0089 & -0.0633 & 0.0160 & -0.0159 & 0.0204 & -0.0068 \\ & 0.4920 & -0.2189 & 0.1147 & -0.1921 & 0.0617 \\ & & 0.3606 & -0.1294 & 0.1531 & -0.1032 \\ & & & 0.2449 & -0.1102 & 0.0945 \\ & & & & 0.2557 & -0.0858 \\ & & & & & 0.1787 \end{bmatrix}_{sym}$
7	$\begin{bmatrix} -0.0104 & -0.0126 & 0.1586 & -0.0494 & 0.0672 & -0.0473 \\ & -0.0035 & -0.1304 & 0.1559 & -0.0764 & 0.1007 \\ & & -0.0135 & -0.1425 & 0.0984 & -0.1152 \\ & & & 0.0472 & -0.1057 & 0.1248 \\ & & & & 0.0207 & -0.0908 \\ & & & & & 0.0577 \end{bmatrix}_{sym}$
8	$\begin{bmatrix} 0 & -1.1960 & 0.6750 & -0.2551 & 0.5571 & -0.1217 \\ & 0 & -1.9351 & 0.0056 & -0.8212 & 0.0031 \\ & & 0 & -1.4098 & 0.0276 & -0.3836 \\ & & & 0 & -1.8090 & 0.0001 \\ & & & & 0 & -1.4807 \\ & & & & & 0 \end{bmatrix}_{skew}$

APPENDIX D

Mathematica Script

```
(* Unsteady Aerodynamics for Deformable Plates *)

(* Plate deformation *)
n = 4;
Do[T[i] = ChebyshevT[i, x], {i, 0, n}];
ψi = 0; Do[ψi = ψi + ci[i] * T[i], {i, 0, n}] ;
w = ψi * τi[t];
v = w + h[t];
Framed[Row[{"v = ", v}], Background → Yellow]
```

$$v = h[t] + \left(ci[0] + x\,ci[1] + \left(-1 + 2\,x^2\right) ci[2] + \left(-3\,x + 4\,x^3\right) ci[3] + \left(1 - 8\,x^2 + 8\,x^4\right) ci[4]\right) τi[t]$$

```
(* Noncirculatory flow *)
σ = (U∞ ∂x v + b ∂t v) // Simplify;
Framed[Row[{"σ = ", Expand[σ]}], Background → Yellow]
```

$$\sigma = ci[1]\,U_\infty\,τi[t] + 4\,x\,ci[2]\,U_\infty\,τi[t] - 3\,ci[3]\,U_\infty\,τi[t] + 12\,x^2\,ci[3]\,U_\infty\,τi[t] -$$
$$16\,x\,ci[4]\,U_\infty\,τi[t] + 32\,x^3\,ci[4]\,U_\infty\,τi[t] + b\,h'[t] + b\,ci[0]\,τi'[t] +$$
$$b\,x\,ci[1]\,τi'[t] - b\,ci[2]\,τi'[t] + 2\,b\,x^2\,ci[2]\,τi'[t] - 3\,b\,ci[3]\,τi'[t] +$$
$$4\,b\,x^3\,ci[3]\,τi'[t] + b\,ci[4]\,τi'[t] - 8\,b\,x^2\,ci[4]\,τi'[t] + 8\,b\,x^4\,ci[4]\,τi'[t]$$

$$\phi nc = \left(int\left[\frac{b}{2\,\pi} \left(\sigma \,/. \,x \to x1\right) \, Log\left[\frac{(x - x1)^2 + \left(\sqrt{1 - x^2} - \sqrt{1 - x1^2}\right)^2}{(x - x1)^2 + \left(\sqrt{1 - x^2} + \sqrt{1 - x1^2}\right)^2}\right] \,// \,\text{Expand}\right]\right.$$

```
        //. int[a_ + b_] :> int[a] + int[b]
        //. int[i_] :> Integrate[i, {x1, -1, 1},
```

$$\text{Assumptions} \to \{-1 <= x <= 1\}, \text{PrincipalValue} \to \text{True}\bigg] \, // \, \text{Simplify};$$

```
Framed[Row[{"ϕnc= ", Collect[(ϕnc), {τi[t], τi'[t], τi''[t], h'[t], h''[t]}, Simplify]}],
  Background → Yellow]
```

$$\phi_{nc} = -b \sqrt{1 - x^2}\,\left(ci[1] - ci[3] + 4\,x^2\,ci[3] + 2\,x\,(ci[2] - 2\,ci[4]) + 8\,x^3\,ci[4]\right) U_\infty\,τi[t] -$$
$$b^2 \sqrt{1 - x^2}\,h'[t] - \frac{1}{30}\,b^2 \sqrt{1 - x^2}\,\left(30\,ci[0] - 20\,ci[2] + 15\,x\,(ci[1] - 2\,ci[3]) +\right.$$
$$\left.30\,x^3\,ci[3] + 4\,x^2\,(5\,ci[2] - 14\,ci[4]) + 8\,ci[4] + 48\,x^4\,ci[4]\right) τi'[t]$$

$$\Delta pnc = \text{Collect}\left[2\,\rho_f \left(\frac{U_\infty}{b}\,\partial_x \phi nc + \partial_t \phi nc\right), \{τi[t], τi'[t], τi''[t], h'[t], h''[t]\}, \text{Simplify}\right];$$

```
Framed[Row[{"Δp_nc = ", Δpnc // Simplify}], Background → Yellow]
```

$$\Delta p_{nc} = \frac{1}{15\sqrt{1-x^2}}$$
$$\rho_f \Big(30\big(-2\,ci[2] + x\,(ci[1] - 9\,ci[3]) + 12\,x^3\,ci[3] + 4\,x^2\,(ci[2] - 8\,ci[4]) + 4\,ci[4] +$$
$$32\,x^4\,ci[4]\big)\,U_\infty^2\,\tau i[t] + 30\,b\,x\,U_\infty\,h'[t] +$$
$$15\,b\big(-3\,ci[1] + 4\,x^2\,(ci[1] - 5\,ci[3]) + 4\,ci[3] + 16\,x^4\,ci[3] + 8\,x^3\,(ci[2] - 6\,ci[4]) +$$
$$32\,x^5\,ci[4] + 2\,x\,(ci[0] - 4\,ci[2] + 8\,ci[4])\big)\,U_\infty\,\tau i'[t] +$$
$$30\,b^2\big(-1 + x^2\big)\,h''[t] + b^2\big(-1 + x^2\big)\big(30\,ci[0] - 20\,ci[2] + 15\,x\,(ci[1] - 2\,ci[3]) +$$
$$30\,x^3\,ci[3] + 4\,x^2\,(5\,ci[2] - 14\,ci[4]) + 8\,ci[4] + 48\,x^4\,ci[4]\big)\,\tau i''[t]\Big)$$

```
(* Circulatory flow *)
K = Collect[Limit[-∂_x ϕnc  1/b √(1-x²) , x → 1],

    {τi[t], τi'[t], τi''[t], h'[t], h''[t]}, Simplify];
Framed[Row[{"K = ", K}], Background → Yellow]
```

$$K = -(ci[1] + 2\,ci[2] + 3\,ci[3] + 4\,ci[4])\,U_\infty\,\tau i[t] - b\,h'[t] - \frac{1}{2}\,b\,(2\,ci[0] + ci[1])\,\tau i'[t]$$

```
Δpc = Collect[2 ρ_f U_∞  1/√(1-x²)  K ( Ck + x (1 - Ck)),

    {τi[t], τi'[t], τi''[t], h'[t], h''[t]}, Simplify];

Framed[Row[{"Δp_c = ", Δpc}], Background → Yellow]
```

$$\Delta p_c = \frac{1}{\sqrt{1-x^2}}\,2\,(Ck\,(-1+x) - x)\,(ci[1] + 2\,ci[2] + 3\,ci[3] + 4\,ci[4])\,U_\infty^2\,\rho_f\,\tau i[t] -$$
$$\frac{2\,b\,(Ck + x - Ck\,x)\,U_\infty\,\rho_f\,h'[t]}{\sqrt{1-x^2}} + \frac{b\,(Ck\,(-1+x) - x)\,(2\,ci[0] + ci[1])\,U_\infty\,\rho_f\,\tau i'[t]}{\sqrt{1-x^2}}$$

```
(* Total pressure difference *)
Δp = Collect[(Δpnc + Δpc), {τi[t], τi'[t], τi''[t], h'[t], h''[t]}, Simplify];
```

```
Framed[Row[{"Δp = ", Collect[(Δp), {τi[t], τi′[t], τi″[t], h′[t], h″[t]}] // Simplify}],
  Background → Yellow]
```

$$\Delta p = \frac{1}{15\sqrt{1-x^2}}$$

$$\rho_f \Big(30\,(-1+x)\,\big(Ck\,(ci[1]+2\,ci[2]+3\,ci[3]+4\,ci[4])+2\,\big(ci[2]+2\,x\,ci[2]+6\,x\,ci[3]+$$
$$6\,x^2\,ci[3]-2\,ci[4]+16\,x^2\,ci[4]+16\,x^3\,ci[4]\big)\big)\,U_\infty^2\,\tau i[t]\,+$$
$$30\,b\,Ck\,(-1+x)\,U_\infty\,h′[t]+15\,b\,(-1+x)\,\big((3+4\,x)\,ci[1]+Ck\,(2\,ci[0]+ci[1])\,+$$
$$4\,(1+x)\,\big(2\,x\,ci[2]-ci[3]+4\,x^2\,ci[3]-4\,x\,ci[4]+8\,x^3\,ci[4]\big)\big)\,U_\infty\,\tau i′[t]\,+$$
$$30\,b^2\,\big(-1+x^2\big)\,h″[t]+b^2\,\big(-1+x^2\big)\,\big(30\,ci[0]-20\,ci[2]+15\,x\,(ci[1]-2\,ci[3])\,+$$
$$30\,x^3\,ci[3]+4\,x^2\,(5\,ci[2]-14\,ci[4])+8\,ci[4]+48\,x^4\,ci[4]\big)\,\tau i″[t]\Big)$$

```
(* Verify Kutta condition: Δp(x=1) = finite *)
Limit[Δp, x → 1] // Simplify
0

(* Generalized aerodynamic force *)
ψj = 0; Do[ψj = ψj + cj[i] * T[i], {i, 0, n}] ;
Q = ⎛  1   ⎞ (int[(Δp * ψj // Expand)]
    ⎝ ρf U∞² ⎠
        //. int[a_ + b_] ⧴ int[a] + int[b]
        //. int[i_] ⧴ Integrate[i, {x, -1, 1}, GenerateConditions → False]);

Framed[Row[{"Q = ", Collect[Q, {τi[t], τi′[t], τi″[t], h′[t], h″[t]}, Simplify]}],
  Background → Yellow]
```

```
Q =
```
$$\pi\,\big(-Ck\,(ci[1]+2\,ci[2]+3\,ci[3]+4\,ci[4])\,(2\,cj[0]-cj[1])-3\,ci[3]\,cj[1]-4\,ci[4]\,cj[1]\,-$$
$$2\,ci[2]\,(cj[1]-cj[2])+3\,ci[3]\,cj[3]+4\,ci[4]\,cj[4]\big)$$
$$\tau i[t]+\frac{b\,Ck\,\pi\,(-2\,cj[0]+cj[1])\,h′[t]}{U_\infty}-\frac{1}{2\,U_\infty}$$
$$b\,\pi\,\big(Ck\,(2\,ci[0]+ci[1])\,(2\,cj[0]-cj[1])+ci[1]\,(2\,cj[0]+cj[1]-2\,cj[2])\,+$$
$$2\,\big(ci[2]\,(cj[1]-cj[3])+ci[4]\,cj[3]+ci[3]\,(cj[2]-cj[4])\big)\big)\,\tau i′[t]\,+$$
$$\frac{b^2\,\pi\,(-2\,cj[0]+cj[2])\,h″[t]}{2\,U_\infty^2}+\frac{1}{240\,U_\infty^2}b^2\,\pi\,\big(-30\,ci[1]\,cj[1]+30\,ci[3]\,cj[1]\,-$$
$$120\,ci[0]\,(2\,cj[0]-cj[2])+20\,ci[4]\,cj[2]+30\,ci[1]\,cj[3]\,-$$
$$45\,ci[3]\,cj[3]-32\,ci[4]\,cj[4]+20\,ci[2]\,(6\,cj[0]-4\,cj[2]+cj[4])\big)\,\tau i″[t]$$

```
(* Lift *)
Lnc = (int[b * Δpnc // Expand]
       //. int[a_ + b_] :→ int[a] + int[b]
       //. int[i_] :→ Integrate[i, {x, -1, 1}, GenerateConditions → False]);
Lc = (int[b * Δpc // Expand]
       //. int[a_ + b_] :→ int[a] + int[b]
       //. int[i_] :→ Integrate[i, {x, -1, 1}, GenerateConditions → False]);
L = Lnc + Lc;

Framed[Row[{"L_nc' = ", Lnc}], Background → Yellow]
Framed[Row[{"L_c' = ", Lc}], Background → Yellow]
```

$$L_{nc}' = -b^2 \pi \, ci[1] \, U_\infty \, \rho_f \, \tau i'[t] - b^3 \pi \, \rho_f \, h''[t] - b^3 \pi \, ci[0] \, \rho_f \, \tau i''[t] + \frac{1}{2} b^3 \pi \, ci[2] \, \rho_f \, \tau i''[t]$$

$$L_c' = -2 \, b \, Ck \, \pi \, ci[1] \, U_\infty^2 \, \rho_f \, \tau i[t] - 4 \, b \, Ck \, \pi \, ci[2] \, U_\infty^2 \, \rho_f \, \tau i[t] -$$
$$6 \, b \, Ck \, \pi \, ci[3] \, U_\infty^2 \, \rho_f \, \tau i[t] - 8 \, b \, Ck \, \pi \, ci[4] \, U_\infty^2 \, \rho_f \, \tau i[t] -$$
$$2 \, b^2 \, Ck \, \pi \, U_\infty \, \rho_f \, h'[t] - 2 \, b^2 \, Ck \, \pi \, ci[0] \, U_\infty \, \rho_f \, \tau i'[t] - b^2 \, Ck \, \pi \, ci[1] \, U_\infty \, \rho_f \, \tau i'[t]$$

```
Framed[Row[{"L' = ", Collect[L, {τi[t], τi'[t], τi''[t], h'[t], h''[t]}, Simplify]}],
 Background → Yellow]
```

$$L' = -2 \, b \, Ck \, \pi \, (ci[1] + 2 \, ci[2] + 3 \, ci[3] + 4 \, ci[4]) \, U_\infty^2 \, \rho_f \, \tau i[t] -$$
$$2 \, b^2 \, Ck \, \pi \, U_\infty \, \rho_f \, h'[t] - b^2 \pi \, (ci[1] + Ck \, (2 \, ci[0] + ci[1])) \, U_\infty \, \rho_f \, \tau i'[t] -$$
$$b^3 \pi \, \rho_f \, h''[t] + \frac{1}{2} b^3 \pi \, (-2 \, ci[0] + ci[2]) \, \rho_f \, \tau i''[t]$$

```
(* Thrust *)
dvdx = D[v, x];
Tp = (int[b * Δp * dvdx // Expand]
       //. int[a_ + b_] :→ int[a] + int[b]
       //. int[i_] :→ Integrate[i, {x, -1, 1}, GenerateConditions → False]);
```

$$S = \frac{\sqrt{2}}{2} K (2 \, Ck - 1) + \text{Limit}\left[\partial_x \phi nc \, \frac{1}{b} \sqrt{1+x}, \, x \to -1\right];$$

```
TLES = π ρ_f b S^2;
Ttotal = TLES + Tp;
```

```
Framed[Row[{"T_LES' = ", Collect[TLES, {τi[t], τi'[t], τi''[t], h'[t], h''[t]}, Simplify]}],
 Background → Yellow]
Framed[Row[{"T_p' = ", Collect[Tp, {τi[t], τi'[t], τi''[t], h'[t], h''[t]}, Simplify]}],
 Background → Yellow]
```

$T_{LES}' = 2 b \pi (-2 (ci[2] + 2 ci[4]) + Ck (ci[1] + 2 ci[2] + 3 ci[3] + 4 ci[4]))^2 U_\infty^2 \rho_f \tau i[t]^2 +$
$2 b^3 Ck^2 \pi \rho_f h'[t]^2 + 2 b^3 Ck \pi (-ci[1] + Ck (2 ci[0] + ci[1])) \rho_f h'[t] \tau i'[t] +$
$\frac{1}{2} b^3 \pi (ci[1] - Ck (2 ci[0] + ci[1]))^2 \rho_f \tau i'[t]^2 +$
$\tau i[t] (4 b^2 Ck \pi (-2 (ci[2] + 2 ci[4]) + Ck (ci[1] + 2 ci[2] + 3 ci[3] + 4 ci[4])) U_\infty \rho_f h'[t] +$
$2 b^2 \pi (-ci[1] + Ck (2 ci[0] + ci[1]))$
$(-2 (ci[2] + 2 ci[4]) + Ck (ci[1] + 2 ci[2] + 3 ci[3] + 4 ci[4])) U_\infty \rho_f \tau i'[t])$

$T_p' = -2 b \pi (4 (ci[2] + 2 ci[4])^2 +$
$Ck (ci[1]^2 - 4 ci[2]^2 + 6 ci[1] ci[3] + 9 ci[3]^2 - 16 ci[2] ci[4] - 16 ci[4]^2)) U_\infty^2 \rho_f \tau i[t]^2 +$
$\tau i[t] (-2 b^2 Ck \pi (ci[1] - 2 ci[2] + 3 ci[3] - 4 ci[4]) U_\infty \rho_f h'[t] - b^2 \pi$
$(ci[1]^2 + 4 ci[2]^2 + 6 ci[3]^2 + Ck (2 ci[0] + ci[1]) (ci[1] - 2 ci[2] + 3 ci[3] - 4 ci[4]) +$
$8 ci[4]^2 + ci[1] (2 ci[2] - 3 ci[3] + 4 ci[4])) U_\infty \rho_f \tau i'[t] -$
$b^3 \pi ci[1] \rho_f h''[t] - b^3 \pi ci[0] ci[1] \rho_f \tau i''[t])$

```
Framed[Row[{"T' = ", Collect[Ttotal, {τi[t], τi'[t], τi''[t], h'[t], h''[t]}, Simplify]}],
 Background → Yellow]
```

$T' = 2 b (-1 + Ck) Ck \pi (ci[1] + 2 ci[2] + 3 ci[3] + 4 ci[4])^2 U_\infty^2 \rho_f \tau i[t]^2 +$
$2 b^3 Ck^2 \pi \rho_f h'[t]^2 + 2 b^3 Ck \pi (-ci[1] + Ck (2 ci[0] + ci[1])) \rho_f h'[t] \tau i'[t] +$
$\frac{1}{2} b^3 \pi (ci[1] - Ck (2 ci[0] + ci[1]))^2 \rho_f \tau i'[t]^2 +$
$\tau i[t] (2 b^2 Ck (-1 + 2 Ck) \pi (ci[1] + 2 ci[2] + 3 ci[3] + 4 ci[4]) U_\infty \rho_f h'[t] +$
$b^2 \pi (-ci[1]^2 + ci[1] (2 ci[2] + 3 ci[3] + 4 ci[4]) +$
$2 Ck^2 (2 ci[0] + ci[1]) (ci[1] + 2 ci[2] + 3 ci[3] + 4 ci[4]) - Ck (2 ci[0] + 3 ci[1])$
$(ci[1] + 2 ci[2] + 3 ci[3] + 4 ci[4]) - 2 (2 ci[2]^2 + 3 ci[3]^2 + 4 ci[4]^2))$
$U_\infty \rho_f \tau i'[t] - b^3 \pi ci[1] \rho_f h''[t] - b^3 \pi ci[0] ci[1] \rho_f \tau i''[t])$

```
(* Power *)
dvdt = D[v, t];
P = (int[b^2 Δp * dvdt // Expand]
      //. int[a_ + b_] :> int[a] + int[b]
     //. int[i_] :> Integrate[i, {x, -1, 1}, GenerateConditions → False]);
```

```
Framed[Row[{"P' = ", Collect[P, {τi[t], τi'[t], τi''[t], h'[t], h''[t]}, Simplify]}],
 Background → Yellow]
```

P' =

$-2 b^3 Ck \pi U_\infty \rho_f h'[t]^2 - \frac{1}{2} b^3 \pi (2 ci[0] + ci[1]) (2 Ck ci[0] + ci[1] - Ck ci[1]) U_\infty \rho_f \tau i'[t]^2 +$

$\tau i[t] \left(-2 b^2 Ck \pi (ci[1] + 2 ci[2] + 3 ci[3] + 4 ci[4]) U_\infty^2 \rho_f h'[t] + \right.$

$\quad b^2 \pi \left(2 ci[2]^2 + 3 ci[3]^2 + 4 ci[4]^2 - ci[1] (2 ci[2] + 3 ci[3] + 4 ci[4]) - \right.$

$\quad\quad \left. Ck (2 ci[0] - ci[1]) (ci[1] + 2 ci[2] + 3 ci[3] + 4 ci[4])\right) U_\infty^2 \rho_f \tau i'[t]\right) -$

$b^4 \pi \rho_f h'[t] h''[t] + \frac{1}{2} b^4 \pi (-2 ci[0] + ci[2]) \rho_f h'[t] \tau i''[t] +$

$\tau i'[t] \left(-b^3 \pi (4 Ck ci[0] + ci[1]) U_\infty \rho_f h'[t] + \frac{1}{2} b^4 \pi (-2 ci[0] + ci[2]) \rho_f h''[t] - \right.$

$\quad \frac{1}{240} b^4 \pi \left(240 ci[0]^2 + 30 ci[1]^2 - 240 ci[0] ci[2] + 80 ci[2]^2 - \right.$

$\quad\quad \left.\left. 60 ci[1] ci[3] + 45 ci[3]^2 - 40 ci[2] ci[4] + 32 ci[4]^2\right) \rho_f \tau i''[t]\right)$

95

REFERENCES

[1]   R. L. Bisplinghoff, H. Ashley, and R. L. Halfman, *Aeroelasticity*. Mineola, 1983.

[2]   W. Shyy, A. Hikaru, C.-K. Kang, and H. Liu, *An Introduction to Flapping Wing Aerodynamics*. New York, 2013.

[3]   C.-K. Kang, H. Aono, C. E. S. Cesnik, and W. Shyy, "Effects of flexibility on the aerodynamic performance of flapping wings," *J. Fluid Mech.*, vol. 689, pp. 32–74, 2011.

[4]   S. Ramananarivo, R. Godoy-Diana, and B. Thiria, "Rather than resonance, flapping wing flyers may play on aerodynamics to improve performance," *PNAS*, pp. 1–6, 2010.

[5]   W. Su and C. King, "Aeroelasticity of Flexible Airfoils with Arbitrary Camber Deformations," *15th Dyn. Spec. Conf.*, no. January, pp. 1–17, 2016.

[6]   R. De Breuker, M. M. Abdalla, and Z. Gürdal, "Flutter of Partially Rigid Cantilevered Two-Dimensional Plates in Axial Flow," *AIAA J.*, vol. 46, no. 4, pp. 936–946, 2008.

[7]   R. Laciga and A. Brown, "Aeroelastic Damping of Turbomachinery Components in a Dense Fluid Medium," University of Liege, 2012.

[8]   L. Huang, "Flutter of Cantilevered Plates in Axial Flow," *Journal of Fluids and Structures*, vol. 9. pp. 127–147, 1995.

[9]   J. Anderson Jr, *Fundamentals of Aerodynamics*, 5th ed. Boston, 2010.

[10]   T. Y.-T. Wu, "Swimming of a waving plate," *J. Fluid Mech.*, vol. 10, no. 3, pp. 321–344, 1960.

[11]   D. Peters and M. Johnson, "Finite-State Airloads for Deformable Airfoils on Fixed and Rotating Wings," *Aeroelasticity Fluid Struct. Interact. Probl. AMSE*, vol. 44, 1994.

[12]   W. P. Walker, "Unsteady Aerodynamics of Deformable Thin Airfoils," Virginia Polytechnic Institute and State University, 2009.

[13]   W. P. Walker and M. J. Patil, "Unsteady Aerodynamics of Deformable Thin Airfoils," *AIAA*, vol. 322, 2010.

[14]   W. P. Walker, "Optimization of Harmonically Deforming Thin Airfoils and Membrane Wings for Optimum Thrust and Efficiency," Virginia Polytechnic Institute and State University, 2012.

[15]   Lord Rayleigh, "On the Instability of Jets," 1878.

[16]   Glauert, "The Elements of Aerofoil and Airscrew Theory," *Cambridge University Press*. Cambridge, 1926.

[17]   R. A. Frazer and W. J. Duncan, "The Flutter of Aeroplane Wings," *Br. A.R.C., R. M. 1155*, 1928.

[18]   Küssner H. G. and Schwarz I., "The Oscillating Wing with Aerodynamically Balanced Elevator," 1941.

[19] T. Theodorsen, "General theory of aerodynamic instability and the mechanism of flutter," *NACA Report*, no. No. 496. 1935.

[20] NASA, "Panel Flutter." 1972.

[21] J. Miles, "On the Aerodynamic Instability of Thin Panels," *J. Aeronaut. Sci.*, vol. 23, no. 8, pp. 771–780, Aug. 1956.

[22] H. C. Nelson and H. J. Cunningham, "Theoretical Investigation of Flutter of Two-Dimensional Flat Panels with One Surface Exposed to Supersonic Potential Flow," *NACA*, 1956.

[23] J. Eisley, "Panel Flutter in Supersonic Flow," California Institute of Technology, 1956.

[24] J. H. Hedgepeth, "Flutter of Rectangular Simply Supported Panels at High Supersonic Speeds," *J. Aeronaut. Sci.*, pp. 563–574, 1957.

[25] E. H. Dowell, "Flutter of Infinitely Long Plates and Shells. Part I: Plate," *AIAA J.*, vol. 4, no. 8, pp. 1370–1377, 1966.

[26] J. Dugundji, E. Dowell, and B. Perkin, "Subsonic Flutter of Panels on Continous Elastic Foundations - Experiment and Theory," 1962.

[27] D. Miller, "Critical Flow Velocities for Collapse of Reactor Parallel-Plate Fuel Assemblies," 1958.

[28] E. B. Johansson, "Hydraulic instability of reactor parallel-plate fuel assemblies," 1959.

[29] G. S. Rosenberg and C. K. Youngdahl, "A Simplified Dynamic Model for the Vibration Frequencies and Critical Coolant Flow Velocities for Reactor Parallel Plate Fuel Assemblies," *Nucl. Sci. Eng.*, vol. 13, no. 2, pp. 91–102, Jun. 1962.

[30] C. Q. Guo and M. P. Païdoussis, "Analysis of hydroelastic instabilities of rectangular parallel-plate assemblies," *J. Press. Vessel Technol.*, vol. 122, no. November 2000, 2000.

[31] L. Schouveiler and C. Eloy, "Coupled flutter of parallel plates Coupled flutter of parallel plates," *Phys. Fluids*, vol. 21, 2009.

[32] S. Michelin and S. G. Llewellyn Smith, "Linear stability analysis of coupled parallel flexible plates in an axial flow," *J. Fluids Struct.*, vol. 25, pp. 1136–1157, 2009.

[33] A. Kornecki, E. H. Dowell, and J. O'Brien, "On the Aeroelastic Instability of Two-Dimensional Panels in Uniform Incompressible Flow," *J. Sound Vib.*, vol. 47, no. 2, pp. 163–178, 1976.

[34] Y. Watanabe, K. Isogai, S. Suzuki, and M. Sugihara, "A Theoretical Study of Paper Flutter," *J. Fluids Struct.*, vol. 16, no. 4, pp. 543–560, 2002.

[35] C. Q. Guo and M. P. Païdoussis, "Stability of Rectangular Plates With Free Side-Edges in Two-Dimensional Inviscid Channel Flow," *J. Appl. Mech.*, vol. 67, pp. 171–176, 2000.

[36] Y. Yadykin, V. Tenetov, and D. Levin, "The Flow-Induced Vibration of a Flexible Strip Hanging Vertically in a Parallel Flow Part 1: Temporal Aeroelastic Instability," *J. Fluids Struct.*, vol. 15, pp. 1167–1185, 2001.

[37] L. Tang and M. P. Païdoussis, "The coupled dynamics of two cantilevered flexible plates in axial flow," *J. Sound Vib.*, vol. 310, pp. 512–526, 2008.

[38] S. Alben, "Simulating the dynamics of flexible bodies and vortex sheets," *J. Comput. Phys.*, vol. 228, no. 7, pp. 2587–2603, 2009.

[39] R. M. Howell, A. D. Lucey, P. W. Carpenter, and M. W. Pitman, "Interaction between a cantilevered-free flexible plate and ideal flow," *J. Fluids Struct.*, vol. 25, no. 3, pp. 544–566, 2009.

[40] S. Michelin, S. G. Llewellyn Smith, and B. J. Glover, "Vortex shedding model of a flapping flag," *J. Fluid Mech.*, vol. 617, pp. 1–10, 2008.

[41] C. Eloy, C. Souilliez, and L. Schouveiler, "Flutter of a rectangular plate," *J. Fluids Struct.*, 2007.

[42] D. Olivier and C. Eloy, "The Influence of Channel Walls on Flag Flutter," *Flow Induc. Vib.*, 2012.

[43] S. Chad Gibbs, I. Wang, and E. Dowell, "Theory and experiment for flutter of a rectangular plate with a fixed leading edge in three-dimensional axial flow," *J. Fluids Struct.*, vol. 34, pp. 68–83, 2012.

[44] S. Heathcote, I. Gursul, D. Martin, and I. Gursul, "Flexible Flapping Airfoil Propulsion at Low Reynolds Numbers," *AIAA J.*, vol. 45, no. 5, pp. 1066–1079, 2007.

[45] S. Heathcote, D. Martin, and I. Gursul, "Flexible Flapping Airfoil Propulsion at Zero Freestream Velocity," *AIAA J.*, vol. 42, no. 11, pp. 2196–2204, 2004.

[46] D. Kodali and C. Kang, "An analytical model and scaling of chordwise flexible flapping wings in forward flight," *AIAA SciTech*, 2016.

[47] M. N. J. Moore, "Analytical results on the role of flexibility in flapping propulsion," *J. Fluid Mech.*, vol. 757, pp. 599–612, 2014.

[48] M. N. J. Moore, "A fast Chebyshev method for simulating flexible-wing propulsion," *J. Comput. Phys.*, vol. 345, pp. 792–817, 2017.

[49] S. Alben, "Optimal flexibility of a flapping appendage in an inviscid fluid," *J. Fluid Mech.*, vol. 614, pp. 355–380, 2008.

[50] S. Michelin and S. G. Llewellyn Smith, "Resonance and propulsion performance of a heaving flexible wing," *Phys. Fluids*, vol. 21, no. 7, pp. 1–21, 2009.

[51] M. J. Shelley and J. Zhang, "Flapping and Bending Bodies Interacting with Fluid Flows," *Annu. Rev. Fluid Mech.*, vol. 43, pp. 449–465, 2011.

[52] J. Weaver, W., P. Timoshenko, S., and H. Young, D., *Vibration Problems in Engineering*, 5th ed. New York, 1990.

[53] J. Katz and A. Plotkin, *Low-Speed Aerodynamics*, 2nd editio. New York, 2001.

[54] D. J. Acheson, *Elementary Fluid Dynamics*, 1st ed. Oxford, 1990.

[55] J. P. Boyd, *Chebyshev and Fourier Spectral Methods*, 2nd ed. Mineola, 2000.

[56] T. von Karman and J. M. Burgers, "General Aerodynamic Thoery-Perfect Fluids," 1935, vol. 2.